



NTNU – Trondheim
Norwegian University of
Science and Technology

Optimizing an Infrared Camera for Observing Atmospheric Gravity Waves from a CubeSat Platform

Snorre Stavik Rønning

Physics

Submission date: December 2012

Supervisor: Patrick Joseph Espy, IFY

Co-supervisor: Robert Hibbins, IFY
Roger Birkeland, IET

Norwegian University of Science and Technology
Department of Physics

0.1 Problem Description

Research characteristics of gravity waves in airglow layer. Based on the wave characteristics, optimize an infrared camera for observing the waves from a CubeSat platform.

0.2 Abstract

The NTNU Test Satellite (NUTS) is a double CubeSat deigned by master students at NTNU. The goal of the project is to image atmospheric gravity waves in the OH airglow layer. This thesis explores the theory behind gravity waves and discuss the design of an infrared camera as a payload onboard. Different requirement based on scientific and mechanical limitations are presented. Based on this a suitable infrared camera is presented.

0.3 Sammendrag

The NTNU Test Satellite (NUTS) er en dobbel CubeSat planlagt og bygget av masterstudenter p NTNU. Målet til prosjektet er ta bilder av atmosfæriske tyngdebølger i OH airglow laget. Denne oppgaven omhandler teorien bak tyngdebølger og hvordan et infrarødt kamera burde bli optimalisert for kunne vre en nyttelast ombord p satelliten. Forskjellige krav basert p vitenskapelige og mekaniske begrensninger er presentert. Basert p denne informasjonen vil et egnet kamera bli presentert.

0.4 List of Acronyms

NUTS NTNU Test Satellite
FOV Field of View
MLT Mesosphere and Lower Thermosphere
GSD Ground Segment Distance
SSP Sub Satellite Point
SWIR Short Wave Infrared
QE Quantum Efficiency
SNR Signal to Noise
FPS Frames per Second

Contents

0.1	Problem Description	1
0.2	Abstract	2
0.3	Sammendrag	3
0.4	List of Acronyms	4
1	Introduction	7
1.1	NUTS - NTNU Test Satellite Project	7
1.2	Observing Atmospheric Gravity Waves	7
1.3	Previous work	8
1.4	Outline	8
2	Theory	9
2.1	Gravity Waves	9
2.1.1	The Air Parcel	10
2.1.2	Buoyancy Frequency	11
2.1.3	Gravity Wave Modeling	11
2.1.4	Gravity Waves in the Airglow layer	15
2.2	Airglow layer	16
2.3	Optical Remote Sensing	18
2.3.1	Resolution Metrics	18
2.3.2	Airglow observation	21
2.4	Signal To Noise Ratio	25
2.4.1	Radiometry	25
2.4.2	SNR	26
2.4.3	Signal	26
2.4.4	Noise	27
3	Analysis and Results	29
3.1	Infrared Camera	29
3.1.1	Scientific Requirements	30
3.1.2	Mechanical Requirements	33

3.1.3	Shock and Vibrations	35
3.1.4	Thermal Vacuum Testing	35
3.2	Intensity Calculation	36
3.2.1	Relative Intensities and Filter	36
3.2.2	Calculating the Intensity	37
3.3	Signal to Noise Results	40
3.3.1	Ideal Case Camera	40
3.3.2	Radiometric Results	40
3.3.3	SNR	42
3.4	Image/Data Acquisition	44
3.4.1	Motion Blur	44
3.4.2	Motion Compensation	47
3.4.3	Observing phase speed	48
3.5	Summary	48
4	Discussion and Future Work	51
4.1	Camera Alternatives	51
4.1.1	OWL	52
4.2	Camera Conclusion	54
4.3	Noise	55
4.3.1	Dark Current	55
4.3.2	Detector	55
4.3.3	Other Noise Sources	55
4.4	Data Processing	55
4.5	Power Consumption	56
4.6	Camera Conclusion	56
4.7	Conclusion	57
5	Appendix	59

Introduction

1.1 NUTS - NTNU Test Satellite Project

The Norwegian University of Science and Technology (NTNU) Test Satellite (NUTS) project is aiming to launch a nanosatellite into Low Earth Orbit (LEO) by 2014. The satellite is a double CubeSat, measuring $10 \times 10 \times 20 \text{ cm}^3$ and weighing less than 2.66 kg, which conforms to the CubeSat standard [13]. The satellite will carry an IR-camera for atmospheric observations as its main payload.

The NUTS project was started in September 2010, and is a part of The Norwegian Student Satellite Program, ANSAT, run by NAROM (Norwegian Centre for Space-related Education)[7]. This program involves three educational establishments, namely the University of Oslo (UiO), Narvik University College (HiN) and NTNU. The program is developed with the intention to stimulate cooperation between different educational institutions in Norway and with the industry. The students will experience team work and hands-on training.

1.2 Observing Atmospheric Gravity Waves

The aim of this thesis will be to optimize an infrared camera in order to research the characteristics of gravity waves in the airglow layer. By obtaining information about the wavelength, phase speed, brightness and orientation of the waves from space, the NUTS will have an opportunity to make a contribution to the ongoing research on gravity waves. In this thesis an investigation on the limitations of an infrared camera onboard a CubeSat platform is performed. The focus have been to acquire the best possible scientific results based on the strict mechanical limitations.

1.3 Previous work

As a member of the NUTS team (from aug. 2011), that have consisted of 10-15 master and project students from different fields of study, a lot of experience have been acquired. Most of the work conducted as a team member have been multidisciplinary. Designing and finding limitations of the payload system have required knowledge about the whole satellite and the subsystems that will affect the payload. To ensure good communications and exchange of information, team meetings have occurred once a week under the leadership of the project manager Roger Birkeland. My role in the team have been to design the payload system in cooperation with Marianne Bakken. The payload system was then divided in two parts: Image analysis and camera research. Mariannes Bakken had the responsibly of the image analysis part and her work can be found in [11].

After the start of the second semester the NUTS participated on the European CubeSat Symposium in Brussels from 30 jan.-1 feb. 2012 with three presentations and one poster. One of the presentations was held by me and Marianne Bakken, and the topic was how to observe atmospheric gravity waves from space with a focus on image analysis.

1.4 Outline

The thesis is built up in the following way. First, chapter 2 will present theory on gravity waves, the airglow layer and the signal to noise calculations. In chapter3 the scientific and mechanical requirements for a camera is analyzed. Calculations of the intensity of the airglow layer and the signal to noise is presented. The effects of motion blur and motion compensation is briefly discussed. In chapter 4 several camera alternatives are presented. There will also be some discussion of noise sources, camera interface and future work. Finally an camera alternative is presented with some analysis.

Chapter 2

Theory

The aim of this chapter is to provide the reader with the necessary background to understand the results and discussions in the following chapters. The theory behind atmospheric gravity waves can be found in section 2.1. Properties of the airglow layer are presented in section 2.2. Basic concepts of remote sensing are presented in section 2.3, and the theory behind the signal-to-noise ratio (SNR) can be found in section 2.4

2.1 Gravity Waves

In fluid dynamics there exist waves that can occur in a medium, or at the interface between two media. When the only restoring force is gravity, these waves are called gravity waves. Waves that oscillate at the surface of the medium are called surface waves, and those that oscillate within are called internal waves. Since the atmosphere can behave like a stable density stratified fluid, internal waves will occur. These internal waves are atmospheric gravity waves. They are quite frequent, and can be found throughout the atmosphere. Depending on their location, the waves will have large variation in both wavelength and frequency. As the waves propagate upwards, they are responsible for momentum and energy transport. This transport can lead to changes in the atmospheric mean flow and triggering of convection and turbulence production [21].

Lack of knowledge about small scale gravity waves has been a limiting factor in numerical climate and weather models. By studying these waves one can contribute to verify and improve future models.

In order to get a further understanding of gravity waves, the air parcel concept and the buoyancy frequency is explained. Gravity waves can also be described with a

set of rather complicated equations called the polarizations relations [10]. It is not within the scope of this thesis to derive the polarizations relations, but the results will be used.

2.1.1 The Air Parcel

The air parcel is a mass of air that is influenced by the environment, but makes no changes to it. The parcel can be viewed as a thin ballon rising and falling adiabatically in a hydrostatic atmosphere. The pressure inside the parcel is equal to that of its surroundings, but the temperature, density and composition can be different. Figure 2.1 illustrate an air parcel rising adiabatically.

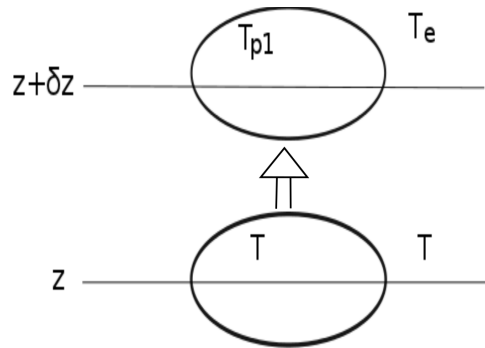


Figure 2.1: Rising air parcel.

When the parcel rises the adiabatic lapse rate changes. The rate is given as $\Gamma_a = \frac{g}{C_p}$, where g is the gravitational acceleration and C_p is the specific heat capacity of air at constant pressure. Equation (2.1) and (2.2) describes the temperature of parcel and its surroundings at altitude $z + \delta z$.

$$T_{p1} = T + \left(\frac{dT}{dz}\right)_{parcel} \delta z = T - \Gamma_a \delta z \quad (2.1)$$

$$T_e = T - \Gamma \delta z \quad (2.2)$$

If $\Gamma \neq \Gamma_a$ then $T_{p1} \neq T_e$.

Since the pressure inside and outside the parcel are equal at $z + \delta z$ we can see from the ideal gas equation (2.3) that the densities are different. If $\Gamma < \Gamma_a$ the parcel is colder than its surroundings and hence a higher density. The parcel will fall and we will have a statically stable atmosphere near z . If $\Gamma > \Gamma_a$ the parcel will be warmer than its surroundings and continue to rise and give a statically unstable atmosphere. We will later see that a stable atmosphere is critical for the creation of gravity waves.

$$\rho_p = \frac{p}{R_a T_{p1}} \quad (2.3)$$

2.1.2 Buoyancy Frequency

The air parcel is rising and falling under the influence of buoyancy. The buoyancy frequency will describe the parcels motion and can be derived from Archimedes' principle:

”Any object, wholly or partially immersed in a fluid, is buoyed up by a force equal to the weight of the fluid displaced by the object.”

-Archimedes of Syracuse

The buoyancy force at $z + \delta z$ is given by:

$$F_b = gV(\rho_e - \rho_p) \quad (2.4)$$

V is the volume of the parcel and ρ_p the density. This force can also be described by Newton's second law:

$$F_b = \rho_p V \frac{d^2(\delta z)}{dt^2} \quad (2.5)$$

Combining equation (2.4), (2.5) and (2.3) gives the following result:

$$\frac{d^2(\delta z)}{dt^2} + N_B^2(\delta z) = 0 \quad (2.6)$$

where

$$N_B^2 = \frac{g}{T}(\Gamma_a - \Gamma)\delta z \quad (2.7)$$

and T is the temperature of the environment. Equation (2.6) describes simple harmonic motion that gives sinusoidal solution if $N_B > 0$, where N_B is the angular frequency. This is only possible if $\Gamma_a > \Gamma$, i.e. the condition of a stable atmosphere is fulfilled. N_B is called the buoyancy frequency or the *Brunt–Väisälä frequency* and will describe the up and down oscillation of the air parcel. This frequency plays an important part in describing the period of gravity waves.

2.1.3 Gravity Wave Modeling

Gravity waves can be generated by flow of air over mountains or frontal systems in the troposphere, see fig.2.2. They can have wavelengths from tens to thousand of km and periods from minutes to hours. The waves differ from normal surface waves in the ocean by the fact that they propagate both vertically and horizontally. Since the kinetic energy per volume ($\frac{J}{m^3}$) is conserved and the density of the

atmosphere is decreasing with altitude, the amplitude of the waves will rise with vertical propagation. They are also special because the propagation of energy (group velocity) is perpendicular to the direction of the wave crests (phase velocity).

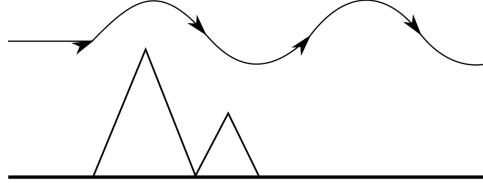


Figure 2.2: A cross-section of a gravity wave formed by air flowing over mountains.

To model gravity waves, one can use the linearised Boussineq equations and find solutions that are plane waves propagating in the x, z plane and independent of y -direction. It has been show in [10] that the dispersion relation for these waves is given by

$$\omega^2 = \frac{N_B^2 k^2}{m^2} \quad (2.8)$$

where ω is the angular frequency, and k and m is the wavenumber in x and z (height) direction.

Form equation (2.8) it is evident that there are two solutions. There is a physical difference between the solutions and this will explain why the phase and group velocity are perpendicular to each other.

The vector group velocity is given by

$$\vec{c}_g = (c_g^x, 0, c_g^z) = \left(\frac{\delta\omega}{\delta k}, 0, \frac{\delta\omega}{\delta m} \right) \quad (2.9)$$

We are interested in the vertical component and by combining (2.8) and (2.9) we get

$$c_g^z = \mp \frac{N_B k}{m^2} \quad (2.10)$$

Since these waves are propagating upwards, i.e. in positive z -direction, we have that $c_g^z > 0$. From equation (2.8) we get that

$$\omega = -\frac{N_B k}{m} \quad (2.11)$$

and by setting $k > 0$ and wanting $\omega > 0$, we get that $m < 0$.

The wave crest and troughs will propagate in the direction the wave-vector $\vec{k} = (k, 0, m)$ and the propagation of energy will go in the direction of the group velocity \vec{c}_g , see figure 2.3.

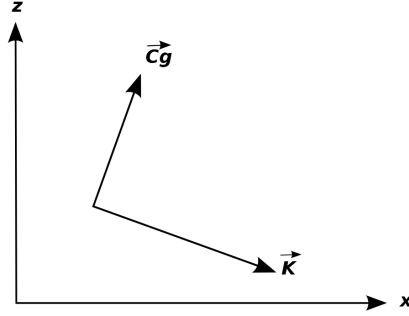


Figure 2.3: A cross section of a gravity wave with group velocity \vec{c}_g and phase velocity in the direction of \vec{k} .

The horizontal wavelengths are usually longer than the vertical ones [10] :

$$\lambda_H > \lambda_V \implies k^2 \ll m^2 \implies \omega^2 \ll N_B^2 \quad (2.12)$$

This shows that gravity waves have an angular frequency much less than the buoyancy frequency N_B . The horizontal scale of the waves are also so small that the effects of Earth's rotation can be ignored. Even for non hydrostatic gravity waves it turns out that $\omega^2 \leq N_B^2$.

The minimum period for gravity waves:

$$T_{min} = \frac{2\pi}{N_B} \quad (2.13)$$

- 8 min for the Troposphere [10]
- 5 min for the Stratosphere [10]

The area of interest for this project is short period waves in airglow layer situated in the Mesosphere and lower Thermosphere (MLT). The typical buoyancy frequency is measured to be $N_B^2 \approx 4 \times 10^{-4} s^{-2}$ [19]. This gives a minimum period of

$$T_{min} \approx \frac{2\pi}{4 \times 10^{-4} s^{-2}} \approx 5 \text{ min} \quad (2.14)$$

Vertical and Horizontal Wavelengths

Figure 2.4 illustrates both the vertical and horizontal wavelengths. The blue and red slopes indicate the rise and fall of an air parcel. The blue line indicates parcels that moves upwards and to the right, in the direction of the group velocity \vec{c}_g . These parcels will have maximum displacement from equilibrium in positive z -direction. When displaced the density of these particles will increase because of adiabatic cooling. The parcels following the red slope will have a displacement downwards and will have a lower density. When they are displaced downwards the parcel will be subject to adiabatic heating.

The relation between the wavelengths [17] is given by

$$\left| \frac{\lambda_v}{\lambda_h} \right| = \left| \frac{\omega}{N_B} \right| \quad (2.15)$$

where ω is the intrinsic frequency of the wave.

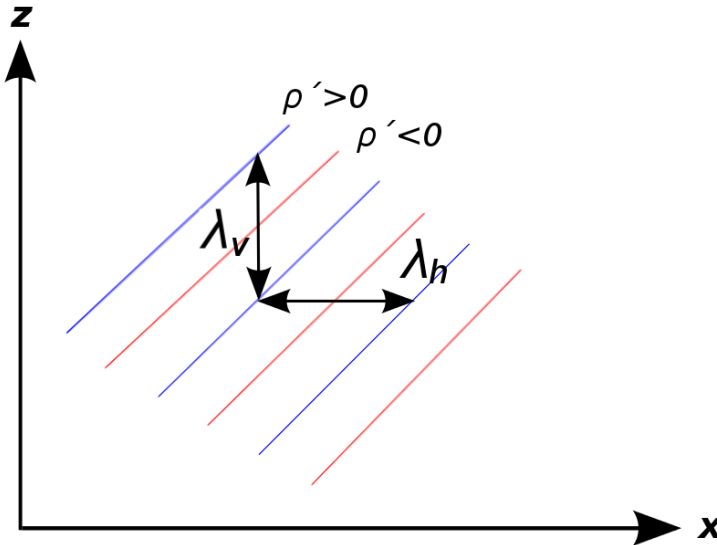


Figure 2.4: A cross-section illustrating the horizontal and vertical wavelengths. The blue and red slopes indicate the rising and falling of the air parcel.

2.1.4 Gravity Waves in the Airglow layer

Intensity Perturbations

As the gravity waves propagate upwards they can eventually reach the airglow layer. When the waves pass through the layer they will create a wave pattern similar to that of rock thrown in a pond. These waves will give rise to an intensity difference in the layer given as

$$\frac{\Delta I}{I} \approx 5\% \quad (2.16)$$

where ΔI is the difference between the top and bottom of a horizontal wave. Note that this is a typical value and that other amplitudes are seen. It is also evident from figure 2.4 that only vertical wavelengths with a wavelength larger than the mean depth (≈ 10 km) of the airglow layer will make detectable perturbations.

Viewing Geometry

Based on the viewing geometry of the satellite, different resolutions of the properties of a gravity wave are achievable. Observation in the nadir direction will often give a large FOV and a high horizontal resolution. This gives the ability to detect small wavelengths. From equation (2.15) we can see that a high vertical to horizontal wavelength ratio will give us the ability to detect high frequency (low intrinsic period) waves.

Observation with a limb view will often have a low FOV and a high vertical resolution. This will result in a low vertical to horizontal wavelength ratio and therefore only low frequency (high intrinsic period) waves are observable. The NUTS will make observations in the nadir direction.

Expected Wave Parameters

Different subsystems of the payload depends on what the camera can expect to see. The number of waves, the average wavelength and the phase speed are all parameters that are important for the calculation of minimum resolution and the motion blur problem. The values used in both this thesis and [11] are based on data from ground observations from Halley, Antarctica (76°S , 27°W) [22], as illustrated in figure 2.5. The mean value for horizontal wavelengths are ≈ 26 km, the observed phase speed have an average of ≈ 48 m/s and the observed period has a mean value of 10 min.

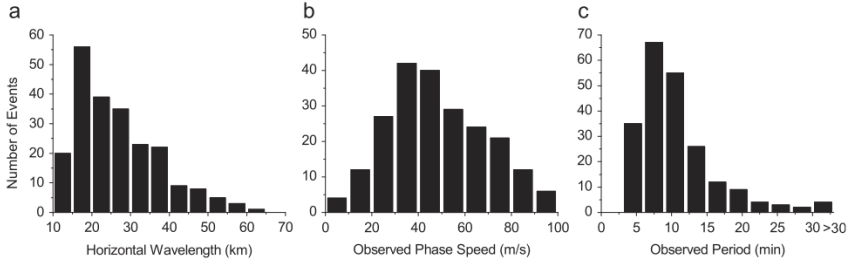


Figure 2.5: Distribution of observed waveparamanters from Halley(2000 and 2001) from [22].

Momentum Deposition

When the waves are propagating upwards they can break and their momentum will be deposited in the mean flow. This will affect the meridional circulation in the mesosphere that will reverse the meridional temperature gradient forced by solar heating at solstices [19].

The waves break because of instability. The instability arises with a large amplitude or when facing a critical layer. A critical layer is when the phase speed of the wave matches the speed of the background wind. The background winds will also give rise to a critical layer filter. If the background wind matches the observed phase speed and direction of a wave, the intrinsic frequency is Doppler shifted to zero and the wave will be absorbed in to the mean flow [22]. This means that the wavelengths will become undetectable.

The momentum flux is given by

$$F_M = \frac{k}{m} \frac{g^2}{N_B^2} \langle \left(\frac{T'}{T}\right)^2 \rangle = \frac{kg^2}{mN_B^2 C_f^2} \langle \left(\frac{I'}{I}\right)^2 \rangle (m^2 s^{-2}) \quad (2.17)$$

where C_f is the cancellation factor that relates the perturbation in temperature to the intensities of the OH layer [19]. There will be both a meridional and zonal momentum flux with seasonal variations.

2.2 Airglow layer

The hydroxyl airglow layer is situated at around 87 km in the Mesosphere and lower Thermosphere (MLT) and emits infrared radiation during the night. The thickness of the layer is around 10 km and the temperature varies throughout the year, from around 150 K in the summer to ≈ 230 K in the winter [20]. The hydroxyl radical (OH) is the neutral form of the hydroxide ion and is highly reactive.

The production of OH in the upper atmosphere occurs during the night when atomic hydrogen reacts with ozone. The production is at its highest five hours after local sunset, and the following equation describes the reaction [23]



The infrared spectrum from OH originates from rotation-vibration transmissions in the excited molecule (OH^*). The emissions can be divided into several bands where each of these bands represent the molecule changing vibrational and rotational levels as illustrated in fig.2.6. From the reaction in equation (2.18) the highest vibrational levels (8 and 9) are produced. The lower levels are produced by collisional quenching or cascading. When the molecules drop to these lower levels, infrared radiation is emitted.

From (2.18) one can see that the production of OH is $\propto [O_3]$ and $[H]$. In a steady state atmosphere, the concentration of O_3 should be constant and the production rate should equal that of hydroxyl. The production of ozone is given by



where M represents a third body that carries off the released energy. The production of both hydroxyl and ozone is proportional to the concentration of atomic oxygen $[O]$. Atomic oxygen is produced during the day according to eq.(2.20). This means that the production of OH ultimately depends on the amount of sunlight.

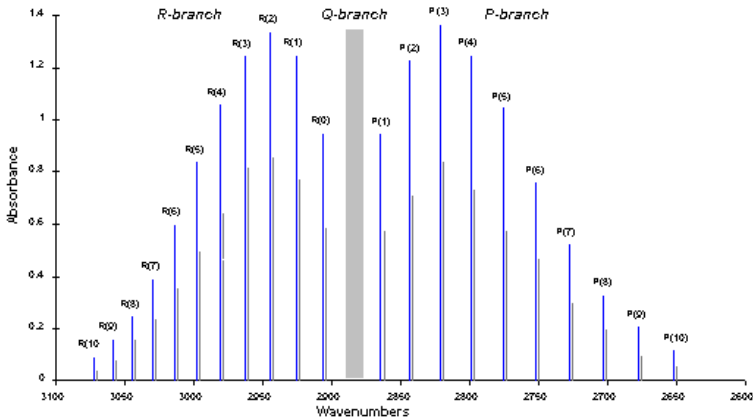


Figure 2.6: Rovibrational transitions of a diatomic molecule. R and P branches indicates bands where the rotational different is $\Delta J = \pm 1$. The Q branch is identified by $\Delta J = 0$. The figure is from [6].

2.3 Optical Remote Sensing

Remote sensing is defined as the science of acquiring information about the Earth without being in physical contact with it. Different types of sensors (active/passive) and techniques (push-broom/whisk broom) can obtain this information, but common for all of them is that the sensing and recording is done by either acoustic waves or electromagnetic radiation.

To find a suitable sensor, one needs to consider the characteristics of the target and the limitations from observers platform. As a main payload in the NUTS project, an infrared camera designed to observe gravity waves in the middle atmosphere is planned. This means that a camera must be chosen with respect to the size, position, speed and intensities of gravity waves in the airglow layer and the size, weight, data and power limitations on the double CubeSat platform.

2.3.1 Resolution Metrics

In order to achieve good image quality and reliable target information one has to consider several factors of the imaging system. One of these factors is resolution. Resolution can be divided into four categories: (1) spatial, (2) spectral, (3) radiometric and (4) temporal. They all have an impact on the final images and several techniques can be applied of the different resolutions in order to improve information from the target.

The infrared camera consist of several subsystems: Optics, detectors, electronics, and electronic imaging system (MTF). Each of these systems usually have their own metrics and each will have different criteria to resolution that affects the choice of camera.

Spatial resolution

Spatial resolution is the measure of how fine detail an image system is able to resolve. In the case of the NUTS project, the spatial resolution will be a measure of the highest spatial frequencies that the system is able to resolve. This will tell us which gravity wave wavelengths can be detected. The spatial resolution will be affected by the properties of the detector and optics.

Ground Sample Distance (GSD)

The GSD is the projection of a detector's pixel pitch onto the ground. The projection is equal to the linear extent that one pixel has the possibility to see. This assumes a fill factor of 100 %, i.e. the percentage of a pixel devoted to capture light. The geometric mean GSD is given by eq.2.21, from [24]

$$GSD = p \frac{H}{f} \left\{ [\cos^2(\beta) + \left(\frac{\sin(\beta)}{\sin(\epsilon)}\right)^2] \times [\sin^2(\beta) + \left(\frac{\cos(\beta)}{\sin(\epsilon)}\right)^2] \right\}^{\frac{1}{4}} \quad (2.21)$$

where p is the pixel pitch, H is the slant range from satellite to airglow, f is the focal length, β is the angle between the x-direction of the sensor and the line perpendicular from the line of sight, and ϵ is the imaging satellite elevation angle.

From fig.2.7, the slant range H is given by

$$H = \sqrt{(R_j + h)^2 - R_j^2 \cos^2(\epsilon)} - R_j \sin(\epsilon) \quad (2.22)$$

where R_j is the distance from center of Earth to airglow layer, and h is the distance from the airglow layer to the satellite.

One can set $\beta = 0$ by assuming that the x-direction of the sensor will be aligned perpendicular to the line of sight. The GSD in nadir direction will then be given by setting $\epsilon = 90^\circ$. For one dimension:

$$GSD_{nadir} = \frac{p \cdot H}{f} \quad (2.23)$$

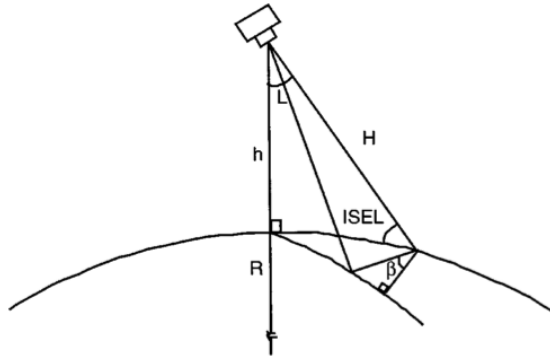


Figure 2.7: Satellite geometry for GSD [24].

With eq.2.23 one can calculate at which height the resolution becomes too coarse to identify different wave patterns or be subject to aliasing. From the Nyquist frequency we get that the GSD should equal half of the wavelength of the GW we want to observe in order to avoid aliasing. That is

$$GSD \leq \frac{\lambda_{GW}}{2} \quad (2.24)$$

Optical resolution metrics

Optical systems are subject to diffraction. Diffraction will contribute to a degeneration of the image quality and produces three factors to be considered: The Rayleigh criterion, Airy disk diameter and the blur diameter.

The Rayleigh criterion and Airy diameter arise from the point spread function [24]. The point spread function describes how a point source of light is spread in an optical system. For a circular aperture it is given by

$$PSF_{optics}(r) = \left[\frac{2J_1(\pi Dr/\lambda f)}{\pi Dr/\lambda f} \right]^2 \quad (2.25)$$

where r is the radius and J_1 is the first order Bessel function.

The Rayleigh criterion is a measure of the ability to distinguish two closely spaced point sources. This is given when the diffraction maximum from one point source corresponds to the first minimum of another point source. The Airy disk will be the diameter of first zero of the PSF and is given as:

$$d_{airy} = 2.44 \cdot \lambda \cdot \frac{f}{D} \quad (2.26)$$

In the optical subsystem it is wise to make d_{airy} roughly the same size as the pixel pitch [14]. If we compare it to the pixel size, we can see that the system is optical limited if $d_{airy} >$ pixel pitch and detector limited if $d_{airy} <$ pixel pitch. The blur diameter is the actual minimum diameter produced by a point source. This can be calculated with ray tracing.

Spectral resolution

Spectral resolution is the ability of a sensor to define fine wavelength intervals. This will measure how good the sensor is to resolve different features in the electromagnetic spectrum. For remote sensing mission carrying a spectrograph this is very important. The infrared camera onboard the NUTS CubeSat will not have this ability and spectral resolution will therefore not be relevant for this project.

Radiometric resolution

The radiometric resolution is commonly known as the gray scale. This is the ability to differentiate between the magnitudes of the incoming energy. A high resolution means that it is easy to discriminate between different energy levels of the incoming radiation. The different energy levels are labeled with a brightness value given by the number of bits representing the energy. The image quality will increase with

the number of bits, but so will the amount of space needed to store the image and how fast the image can be stored (system bus).

The radiometric resolution will also depend on the spectral resolution. A high spectral resolution will give a small GSD and less energy will be detected, resulting in a lower radiometric resolution. The resolution will depend on the well depth and the quantization levels of the detectors. The well depth will tell the amount of intensity (counts) the detector can handle before it is saturated. Saturation will lead to image defects such as blooming.

Temporal resolution

Temporal resolution is the measurement accuracy with respect to time. There will be two types of temporal resolution, one for the sensor and one for the platform. For a sensor the resolution is the sampling time and often described by the update frequency (Hz). This will be limited by the amount of data storage available. The temporal resolution for a satellite will be the revisit time, i.e. the time it takes for the satellite to image the exact same area again. The revisit time depends on the satellite orbit, ADCS system and the position of the target. For a satellite with a polar orbit and a target located at high latitude, the revisit time will most likely be a couple of hours.

2.3.2 Airglow observation

In order to observe the airglow layer other factors than resolution must be considered. These include the orbit, data transmissions, pointing accuracy, atmospheric absorption and image quality.

Orbit

The orbit of the NUTS will be a sun-synchronous orbit with an inclination of 98° and an altitude of ≈ 600 km. The orbit will pass above the poles, and will have the possibility to cover large areas of the airglow layer. One advantage of the sun-synchronous orbit is that it allows the satellite to pass over a specific area at the same local mean solar time.

As the Earth revolves around the Sun, the sun synchronous orbit is maintained if it precess at the same rate as Earth. Because of the oblate shape of Earth, a torque will be acting upon the satellite. It is shown that an inclination of 98 degrees (8 degrees off the poles) will give rise to a torque that for a height of around 600-800 km gives the desired precession. At this height the period will be around 96-100 min. For the NUTS CubeSat, the expected number of revolutions per day is 15.

There are two special cases of the sun synchronous orbit: noon/midnight and dawn/dusk. Noon/midnight is the orbit when the local mean solar time of passage

for equatorial longitudes are either at noon or midnight. A dawn/dusk orbit will place the satellite between day and night, i.e. the local mean solar time will be either sunrise or sunset. This orbit is not an option for the NUTS CubeSat. Radiation from the illuminated parts of Earth's surface would disturb the camera and since the airglow radiates during the night, the camera would not get the possibility of taking images in the nadir direction. By pointing the camera at the night side this could be avoided. This would on the other hand put high requirements on the ADCS-system and it may not provide us with the proper information compared to that of a nadir view.

Future investigation into the final orbit should be to consider when the camera is positioned over a specified area around five hours after local sunset. This is the time when the intensity of the airglow is at its strongest [23]. It is also preferable to target areas where there exist ground observations sites.

Data transmission

The downlink of NUTS is 9600 bit/s, and approximately half of this will be house-keeping data and the other half dedicated to the payload. It has been shown in [11] that on average the expected payload data will be around 2.45 Mb/day. This will correspond to around 4 uncompressed images with a 320×256 resolution.

Pointing accuracy

Figure 2.8 illustrates the geometry of airglow viewing in two dimensions. From this figure we can calculate the "horizon" of the camera, that is the area that the satellite can point its sub satellite point (SSP). The geometric relation is:

$$\sin(\rho) = \frac{R_e + H_{OH}}{R_e + H_{sat}}$$

using the values: $R_e = 6371$ km, $H_{OH} = 90$ km and $H_{sat} = 630$ km,

$$\rho \approx 67^\circ \tag{2.27}$$

This means that if the SSP is pointed 67° from nadir, the SSP will "miss" the atmosphere. Before this the camera would already have started to "see" space. This means that infrared radiation from other sources than the atmosphere will be detected. In order to avoid this, a pointing accuracy limit has to be defined. As long as the satellite points within this angle, the camera will only detect radiation from the airglow layer.

The pointing accuracy limit is defined as:

$$P_A = \rho - \frac{FOV}{2}$$

No disturbing radiation will be detected as long as the SSP is pointed within the P_A . The ADCS system on the satellite can provide a pointing accuracy within 10° of nadir.

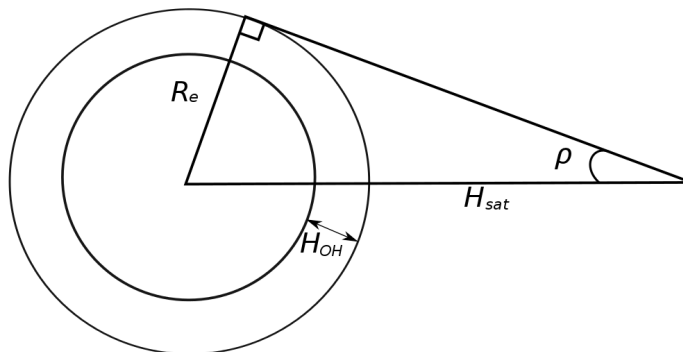


Figure 2.8: Atmospheric viewing geometry.

Atmospheric Absorption

The absorption of different atmospheric gases is illustrated in fig.2.9. Observation of the airglow layer will be at $1.45 \mu\text{m}$. The advantage of observing at this wavelength is the zero transmittance provided by water vapour.

Water vapour plays a key role in our atmosphere and around 99% is found in the troposphere. The interactions between water vapour and infrared radiation will affect the design of the payload.

The water molecule (H_2O) is a triangle triatomic molecule consisting of one oxygen and two hydrogen atom. The molecule is an asymmetric rotator and has three fundamental modes of vibration fig.2.10. These modes are responsible for the absorption. From figure 2.10 we see that the water vapour is situated well below the airglow layer and this works to NUTS' advantage. Since water absorbs the $1.45 \mu\text{m}$ radiation from Earth, this will not be visible for the camera. The radiation from the airglow layer consists of different wavelengths, but with the right filter one can detect radiation with a wavelength of $\approx 1.45 \mu\text{m}$.

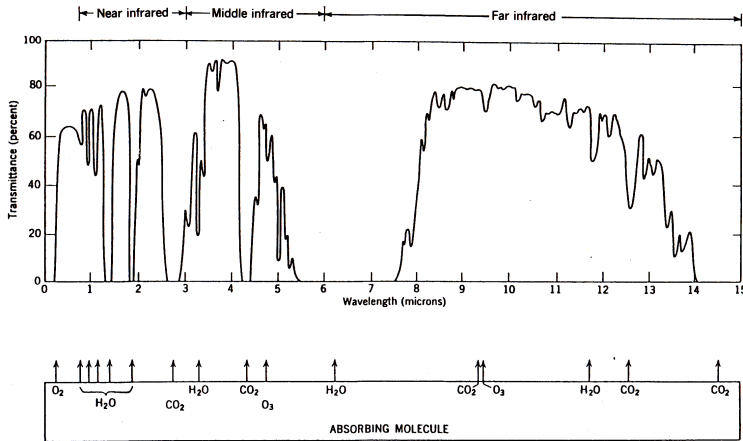


Figure 2.9: Transmittance vs. wavelength from [16].

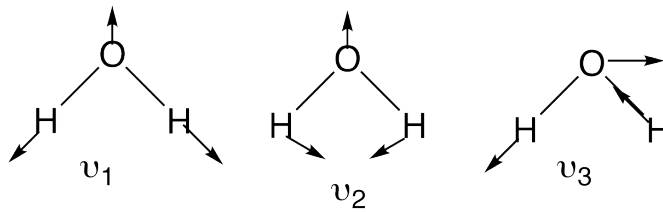


Figure 2.10: Fundamental vibrational modes of a water molecule[4].

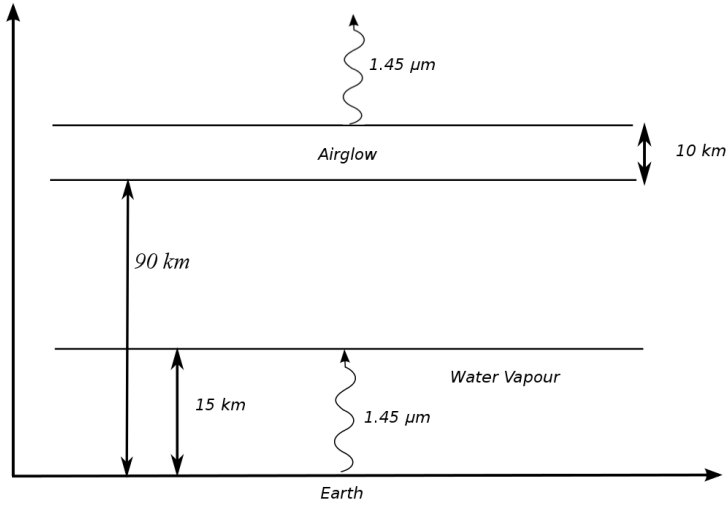


Figure 2.11: Illustration of how the water vapour is situated relative to the airglow layer. Water vapour absorbs the 1.45 μm radiation.

2.4 Signal To Noise Ratio

The SNR ratio is a common metric used in different fields in both science and engineering. SNR is defined as the power ratio between a signal and the background signal (noise). In this thesis the SNR will be used to describe the radiometric performance and the image quality of an infrared camera.

2.4.1 Radiometry

The SNR can be calculated if one knows the amount of photons hitting the detector. From [14] the number of photons is given by

$$n_{DETECTOR} = \int_{\lambda_1}^{\lambda_2} \frac{\pi}{4} \frac{L_q(\lambda) A_D}{F^2 (1 + M_{OPTICS}^2)} T_{OPTICS}(\lambda) T_{ATM}(\lambda) t_{int} d\lambda \quad (2.28)$$

L_q = Spectral photon radiance ($\frac{\text{photons}}{\text{m}^2 \cdot \text{s} \cdot \mu\text{m} \cdot \text{sr}}$)

A_D = Detector Area

T_{OPTICS} = Optical transmission

T_{ATM} = Atmospheric transmission

t_{int} = Integration time (s)

F = F-number

M_{optics} = Optical magnification

The relationship between the photon radiance and the photon flux is given by

$$L = I \frac{10^{10}}{4\pi} \quad (2.29)$$

where I is intensity in Rayleigh.

2.4.2 SNR

The basic definition of SNR is

$$\text{SNR} \equiv \frac{\text{signal}}{\text{noise}}$$

but a more accurate one is necessary for this project. To get the relevant data, it is critical to detect the mean signal difference produced by the gravity wave perturbations. This means that the payload must distinguish between the intensities of the wave crests and troughs, see section 2.1.4

The following definition will be used

$$\Delta\text{SNR} = \frac{\text{signal}_{\text{wavetop}} - \text{signal}_{\text{wavebottom}}}{\text{noise standard deviation}} = \frac{\Delta s_{\text{target}}}{\sigma_{\text{noise}}}$$

2.4.3 Signal

[26] gives the signal of interest produced by the detector as

$$\Delta s_{\text{target}} = \Delta P \cdot Q_e \cdot t_{\text{int}} \quad (2.30)$$

P = photon flux ($\frac{\text{photons}}{\text{pixel} \cdot \text{seconds}}$)

Q_e = Quantum efficiency ($\frac{\text{electrons}}{\text{photon}}$)

The ΔP is difference in the amount of photons hitting the detector per pixel.

$$\Delta P = \frac{n_{\text{wavetop}} - n_{\text{wavebottom}}}{\text{Number of pixels}} = \frac{\Delta n_{\text{detector}}}{\text{Number of pixels}}$$

How to increase the signal will be further discussed in results, but one technique that can be applied at this level is binning. This will lower the amount of pixels on the detector, resulting in a lower spatial resolution and an increase in dark current.

The quantum efficiency (Q_e) is a measure of the average amount of electrons generated by photons at the detector. It is wavelength dependent and is often illustrated as figure 2.12

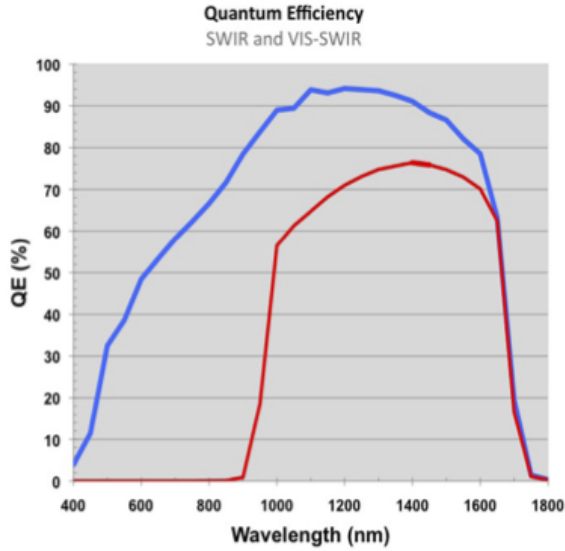


Figure 2.12: Quantum efficiency from [3].

2.4.4 Noise

Noise can be classified as undesirable signal components that will degrade the performance of the detector. There exists many sources of noise, but only the most relevant will be discussed. If the different sources of noise can be considered independent [24] and they each follow a normal distribution the standard deviation of noise is

$$\sigma_{noise} = \left(\sum_{n=1}^N \sigma_n^2 \right)^{\frac{1}{2}} \quad (2.31)$$

The three different types of noise consider the major contributors are photon, dark and read noise.

Photon Noise

The photon noise (shot noise) is a consequence of the statistical variation (random fluctuations) in the arrival rate of photons on the detector. This noise will be Poisson distributed, but for a large signal it can be approximated as a normal distribution where the standard deviation will be

$$\sigma_{photon} = \sqrt{signal_{target} + signal_{background}} \approx \sqrt{\Delta s_{target}} \quad (2.32)$$

In our case of airglow observation the $signal_{background} \approx 0$. This is because of the filtering effect provided by the water vapour layer as described in section 2.3.2.

Dark Noise

Dark noise results from the statistical variation in thermally generated electrons in the detector when no light is incident on the detector. The rate at which these electrons are created is called dark current and is highly temperature dependent. Cooling the detector will reduce the dark noise. Dark noise is Poisson distributed and the standard deviation is given by

$$\sigma_{dark} = \sqrt{\bar{i}_{dark} \cdot t_{int}} \quad (2.33)$$

where \bar{i}_{dark} is the average dark current and is usually measured for different temperatures.

Read Noise

The "reading" of electrons generated by the photons occurs in two steps. At first the electrons have to be converted into a voltage signal, and then this signal has to be quantified. Read noise is the combination of the noise at two steps. Since multiple analog signals can be represented by one digital value, noise will arise. This will depend on the amount of electrons that can be stored at one pixel $N_{welldepth}$ and the number of digital counts N_{DR} . It is assumed that the number of electrons per digital count will be normal distributed and from [24] we get a standard deviation

$$\sigma_{quantization} = \frac{N_{welldepth}}{N_{DR}\sqrt{12}} \quad (2.34)$$

Read noise is usually provided in data sheets as a *electrons/count*

Chapter 3

Analysis and Results

This chapter provides the analysis and results for different elements that are crucial in order to attain the desired information about gravity waves. Section 3.1 presents the scientific and mechanical requirements for the camera. In section 3.2, the method for calculating the expected intensity of the airglow layer is presented. Based on data from the previous sections, section 3.3 present the calculation of the expected signal to noise ratio. Section 3.4 presents the limitations for data acquisition. This is based on the effects of motion blur and motion compensation.

Note that some of the results in this chapter is based on parameters that depend on each other. Due to the complex dependencies, an ideal camera is constructed in section 3.3. This will simplify some calculations, but it is not expected that the final camera will have the same parameters as this camera. The intention of the calculations is to provide guidelines for future work, and provide results that can be used to make sure that the final camera is the most suited one for this project.

3.1 Infrared Camera

The infrared camera will be the main payload onboard the NUTS, and the goal is to take images of gravity waves in the airglow layer. Based on these images one hopes to extract information about the wavelength, phase speed and orientation of the waves. Infrared cameras are usually designed for a specific use, and since the NUTS project philosophy is to use off-the-shelf electronics, one have to make sure that a commercial camera can provide the scientific data. In addition to this, the platform and the camera will both be subject to extreme conditions that the majority of electronic systems are not designed for. The following sections describes the scientific and mechanical requirements that a suitable camera must meet.

3.1.1 Scientific Requirements

The infrared radiation that the camera will detect originates from the OH(2,0), OH(3,1) and OH(9,6) bands. The wavelength range of the bands are from 1.3 -1.7 μm . In order to register these wavelengths, the detector has to be made of indium gallium arsenide (InGaAs). The majority of commercial SWIR cameras have a sensitivity from 0.9-1.7 μm , but the range can be extended up to $\approx 2.6 \mu\text{m}$ by changing the ratio between In and Ga [8].

Focal length

From section 2.1.4, the mean wavelength of gravity waves is found to be $\lambda_{GW} \approx 26$ km. To avoid aliasing of the waves, the correct value of GSD must be obtained. This is given as

$$GSD \leq \frac{\lambda_{GW}}{2} \approx 13 \text{ km} \quad (3.1)$$

From figure 2.5, one can see that by making sure the GSD is lower than 13 km, provide the possibility to observe the majority of wavelengths. Based on a camera with a pixel pitch $p \approx 30 \mu\text{m}$ at a height of $H = 600$ km, the minimum focal length necessary to produce this resolution is acquired by combining the result in eq.(3.1) with eq.(2.23). This will be the minimum focal length, and it is strongly advised to have a larger one.

$$f = \frac{p \cdot H}{GSD_{nadir}} \approx 1.4 \text{ mm} \quad (3.2)$$

Systems with a large focal length will achieve a high resolution, but this will limit the FOV. Since a large FOV provides a large area to detect, the possibility to detect gravity waves will increase with the FOV. The FOV can be derived from figure 3.1 and is given as

$$FOV = 2 \cdot \alpha = 2 \cdot \arctan\left(\frac{N_{pix} \cdot GSD}{2H}\right) \quad (3.3)$$

where α is the view in radians, N_{pix} is the number of pixels on the detector in either horizontal or vertical direction, and H is the height of the satellite. Combining eq.(3.2) and eq.(3.3) will result in

$$FOV = 2 \cdot \arctan\left(\frac{N_{pix} \cdot p}{2f}\right) \approx \frac{N_{pix} \cdot p}{f} \quad (3.4)$$

This equation will describe how the FOV will vary with focal length, and the results are plotted in fig.3.3.

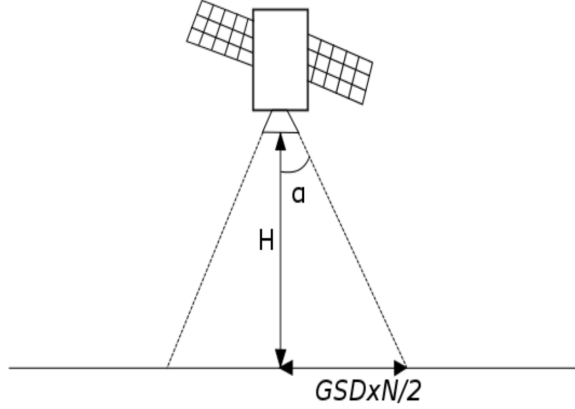


Figure 3.1: Illustration of the FOV geometry.

Resolution

The GSD is given by eq.(2.21) and eq.(2.22) in section ???. To find how the GSD will vary with an off nadir view, the elevation angle must be converted into the looking angle. The looking angle L is related to elevation angle ϵ by the relation:

$$\sin(L) = \frac{R_j}{R_j + h} \cos(\epsilon) \quad (3.5)$$

where R_j is the distance from center of earth to airglow layer, and h is the distance from the airglow layer to the satellite [15]. From eq.(3.5) the following equations can be obtained

$$\cos(\epsilon) = \frac{R_j + h}{R_j} \cdot \sin(L) \quad (3.6)$$

$$\sin(\epsilon) = \sqrt{1 - \left(\frac{R_j + h}{R_j} \cdot \sin(L)\right)^2} \quad (3.7)$$

Substituting them into eq.(2.21) and eq.(2.22) provides the following results,

$$H(L) = (R_j + h) \sqrt{1 - \sin^2(L)} - R_j \sqrt{1 - \left(\frac{R_j + h}{R_j} \cdot \sin(L)\right)^2} \quad (3.8)$$

and

$$GSD(L) = p \frac{H(L)}{f} \left\{ \left[\cos^2(\beta) + \left(\frac{\sin(\beta)}{\sqrt{1 - \left(\frac{R_j + h}{R_j} \cdot \sin(L)\right)^2}} \right)^2 \right] \times \left[\sin^2(\beta) + \left(\frac{\cos(\beta)}{\sqrt{1 - \left(\frac{R_j + h}{R_j} \cdot \sin(L)\right)^2}} \right)^2 \right] \right\}^{\frac{1}{4}} \quad (3.9)$$

Equation (3.8) provides the slant range, and eq.(3.9) will describe how the GSD will change based on the looking angle and the orientation of the detector (relative to the direction of the satellite). The plot of eq.(3.9) is shown in figure 3.2, and is based on a camera with pixel pitch $p = 30 \mu m$, and a focal length of $f = 16 \text{ mm}$.

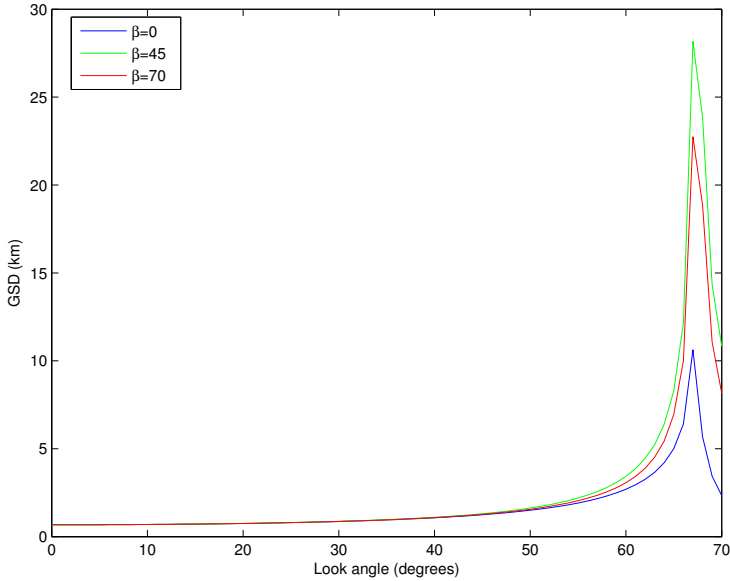


Figure 3.2: The GSD as a function of look angle and detector orientation (β).

In figure 3.2, the GSD change drastically for looking angles of $L > 60$. This corresponds well to the limit for sub satellite point at 67° from section 2.3.2. Since the look angle will be far from 67° , it is also clear that the orientation of detector can be neglected. For $L < 60$, the GSD will be approximately the same as in the nadir direction, which is far below the requirement set by eq.(3.1). Because of the low influence of the looking angle, the GSD can be simplified to that of the nadir direction.

$$GSD = \frac{p \cdot H}{f} \quad (3.10)$$

Figure 3.3 is plot of eq.(3.4) and eq.(3.10). The figure illustrates how the focal length affects the FOV and GSD. The pixel pitch is $30 \mu m$, and number of pixels is 320. The highest GSD the focal length can provide is well below the NUTS requirements. Based on this, the choice of focal length should be based on the desired FOV.

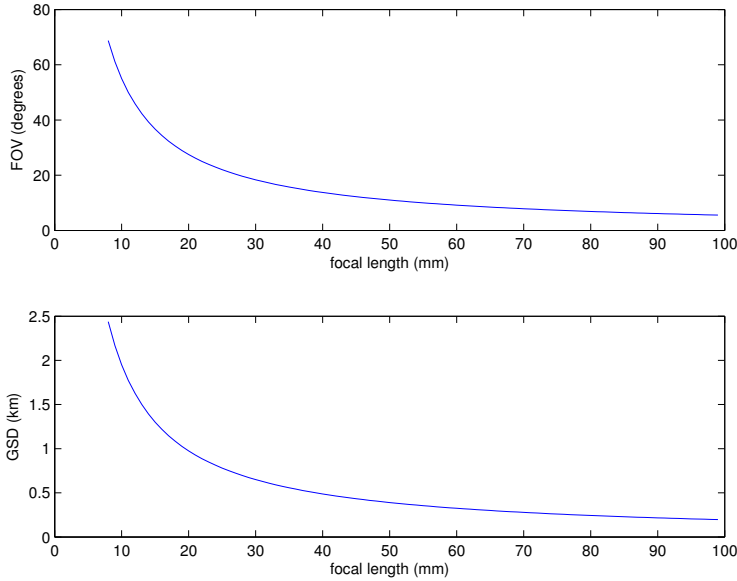


Figure 3.3: FOV and GSD_{nadir} vs. focal length.

The accuracy provided by the ADCS system is 20° [25]. From section 2.3.2, the maximum FOV can then be

$$FOV_{max} = 2 \cdot (\rho - P_{A_{min}}) = 2 \cdot (67^\circ - 20^\circ) = 97^\circ \quad (3.11)$$

The FOV in the previous calculations is done for only one side of the detector. If the detector is quadratic, i.e. the number of pixels in the x-direction equals that y-direction, the FOV will be the same. If this is not the case, one would have to do similar calculations for the y-direction.

3.1.2 Mechanical Requirements

The size and weight restrictions are the limiting factors of the physical requirements. The dimension of the NUTS platform is given by the CubeSat standard [13]. This limits the size to $100 \times 100 \times 100 \text{ mm}^3$, and the total mass to 2.6 kg. Figure 3.4 illustrates the interior of the satellite and the black area is the position of the camera. It is important for the satellite that the center of mass is within the CubeSat standard. The satellite will be subject to different forces during the launch, and will face an extreme environment in space. To make sure the satellite will function properly under harsh conditions, a number of tests have to be done preflight. The HinCube from Narvik University College have already been through

the tests and it is expected that the NUTS will face the same. To be prepared for space, the satellite will have to go through shock, vibration and thermal vacuum tests. Based on the test data from HinCube, several camera requirements can be identified.

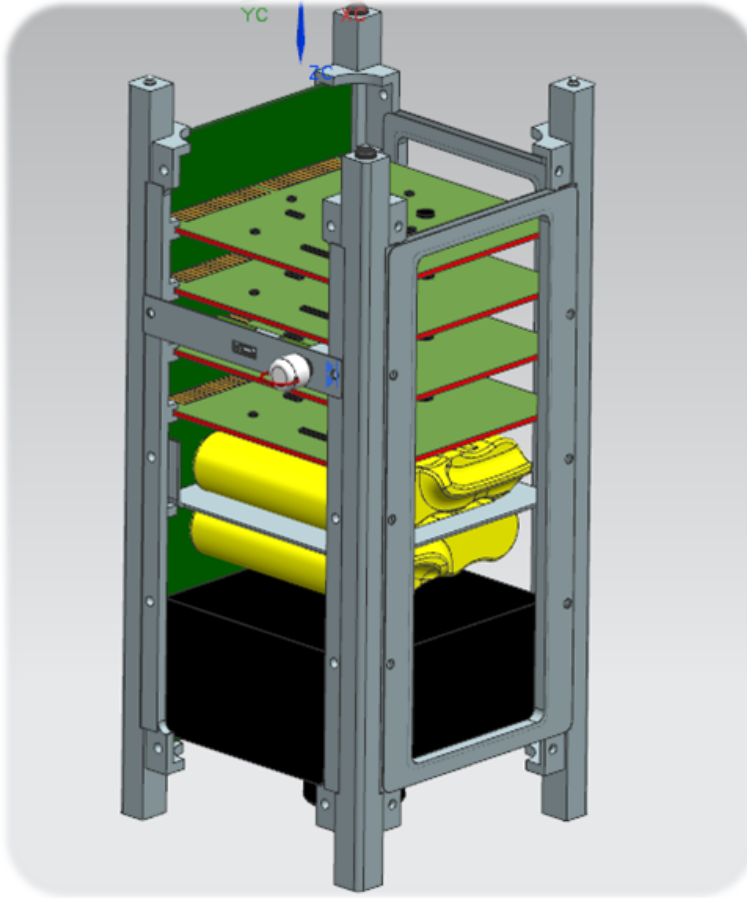


Figure 3.4: The black area illustrates the payload position. Courtesy of Kim Sandvik.

Size and Weight

The absolute size restrictions for the payload system is given in fig.3.5. The camera has to fit in a box of $92 \times 88 \times 65 \text{ mm}^3$, where the lens can stick 8.6 mm out of the box. The maximum diameter of the lens can only be 35 mm. This is because of limitations set by the radio system on that part of the satellite. The mass budget is not yet in place for the satellite (December 2012), but the total weight of the

camera should be between 200-300 g. This will correspond to around 10% of the total weight. There could arise a situation where the weight of the camera will move the center of mass so much that counter weight would have to be applied on the opposite side of satellite. Depending on the interface of the camera, the available space might also include a FPGA and a flash memory. There will also be some challenges related to the mounting of the camera, but this is beyond the scope of this thesis.

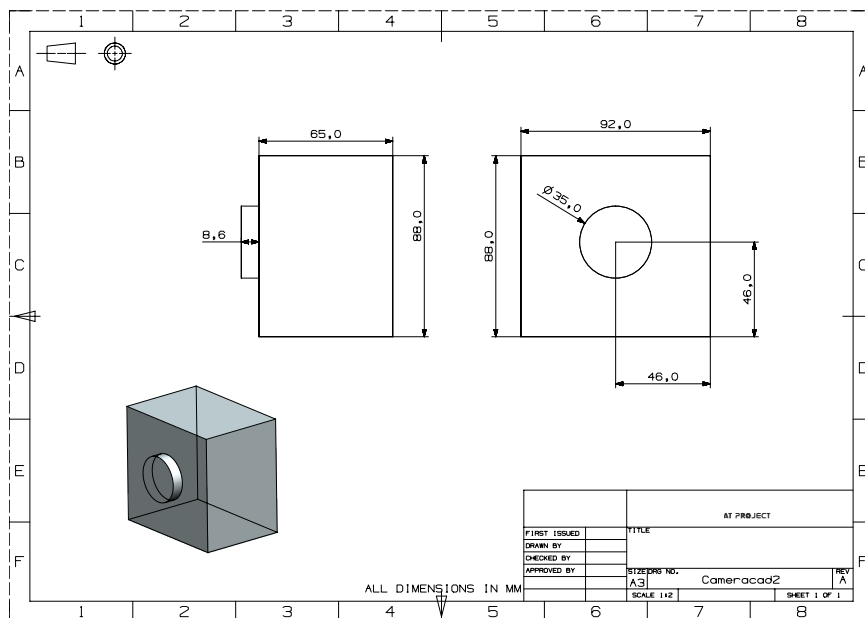


Figure 3.5: Sketch of the size criterions, made by Kim Sandvik.

3.1.3 Shock and Vibrations

During the launch, different forces can cause several malfunctions to the satellite system. To simulate what the satellite will experience, shock and vibrations test are done preflight. Based on the test done to the cubesat from Narvik University College HinCube, several criteria are listed in table 3.1. The details of these tests are described in ???. The values in 3.1 will be used as guidelines in the selection of a camera. One problem is that camera producers don not provide this data in the technical information.

3.1.4 Thermal Vacuum Testing

During its orbit, the satellite will be subject to temperatures ranging from -20°C to 20°C [12]. The camera will only operate during the night, so good functionality for

Table 3.1: Shock and Vibration Criteria

Test	Frequency	g-force
Shock	80-125 Hz	10 g
Vibration	5-20 Hz	1 g

low temperatures is critical. The operating temperature range is usually provided by the manufacturer, and should be within the satellites temperature range.

In addition to the low temperature range, the camera will also operate in approximately vacuum. This will cause an outgassing of materials, and commercial cameras are usually not tested for this. Some manufacturers do on the other hand have previous experience with delivering cameras for missions in space and can provide data. From the thermal vacuum test of HinCube, a bake out test is performed with the test parameters in table 3.2. The details of the test can be found in [1].

Table 3.2: Parameter Bakeout

Characteristics	Proto-flight
Vacuum level	10^{-5} bar
Temperature	+ 60 ° C
Duration	24 h

3.2 Intensity Calculation

3.2.1 Relative Intensities and Filter

The intensity of the airglow layer is an important parameter in the SNR calculation. A plot of the OH intensity based on the data from [18] can be seen in fig.3.6. The range is 1.3 -1.7 μm and correspond to a section of the range that many commercial SWIR cameras offer. The sensitivity of SWIR cameras usually start at 0.9 μm and continue to a relative sharp cut-off at $\approx 1.7 \mu\text{m}$.

The aim of the NUTS project is to study airglow radiation from the OH(2,0), OH(9,6), and OH(3,1) bands at a wavelength of $\approx 1.45\mu\text{m}$. The relative values of these bands are plotted in fig.3.6. From this it is clear that the (9,6) band, which is barely visible, is significantly weaker than both the (2,0) and (3,0) band. The filter response will provide data for the total radiation received at the detector.

The optical filter is modeled as a normal probability density distribution, with a mean $\mu = 1.45$, and standard deviation of $\sigma = 0.025$. This will correspond to a range from ≈ 1.4 -1.5 μm . The transmittance of the filter is $\approx 70\%$, and the result is shown in fig.3.6. The filter response is the convolution between the intensity values

and the filter. This will provide the data for the intensity received at the detector. For the relative intensities in fig.3.6, the filter response is plotted in fig.3.7.

A real filter will have a different filter response, but fig.3.7 illustrates what to be expected, and what type of filter to look for. The reason to study the radiation at $1.45 \mu\text{m}$ is water's ability to absorb at this wavelength. Radiation from both Earth and the airglow layer will be absorbed at this wavelength. For the satellite this is an advantage since "noise" from Earth will vanish, but for ground based detectors this wavelength will not be visible. Positioning an optical filter at $1.45 \mu\text{m}$ will maximize the natural filter provided by water vapour.

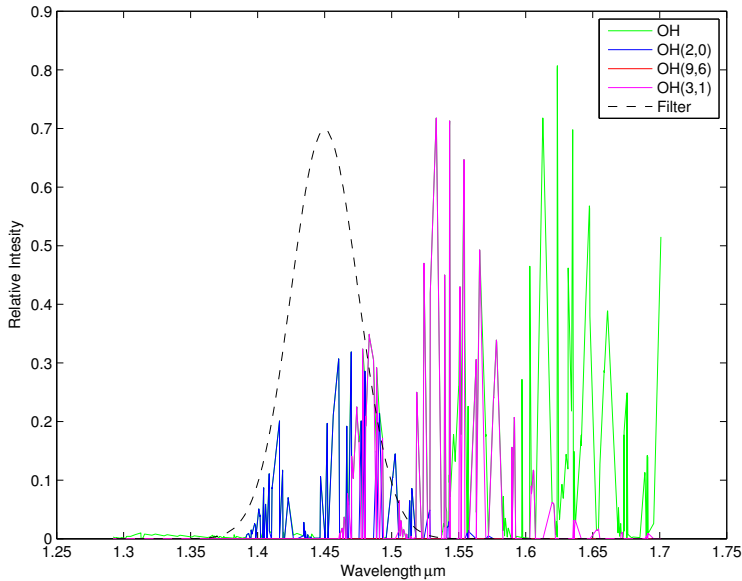


Figure 3.6: Intensities for OH bands, and the optimal location for the filter. The value of the filter is not to scale, and the continuous values of the radiation are there to illustrate the position easier. The values are actually discrete.

3.2.2 Calculating the Intensity

The intensities provided by [18] are relative to each other. To calculate the intensities for different bands, these values have to be normalized to the appropriate band. Because the intensity of a band will vary with both latitude and season, the normalization provides the possibility to scale the values with the averaged intensity for a certain location. So if the camera could see a whole band, the received intensity would be the average intensity of that band. The normalization is given

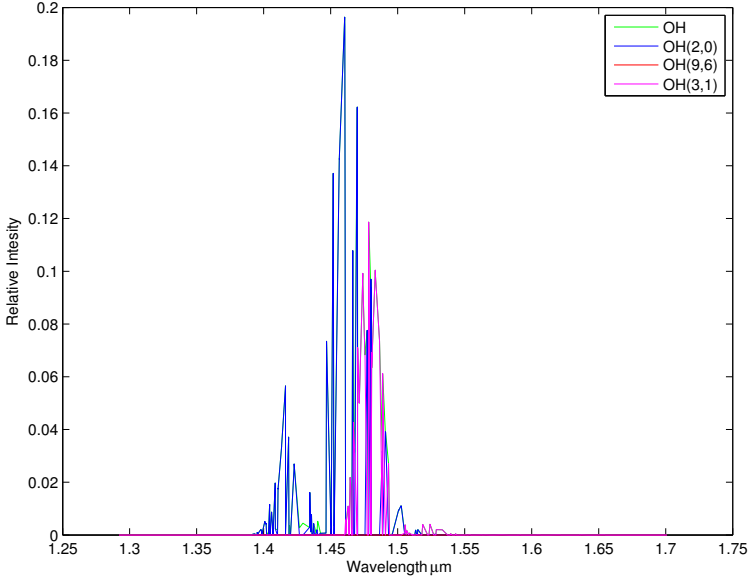


Figure 3.7: Filter response for the relative intensities.

as

$$I(n) = \frac{I'(n)}{\sum I'(n)}$$

where $I'(n)$ is the relative intensity at a given wavelength for a certain band, and $\sum I'(n)$ is the sum of the relative intensities of that band, e.g. the OH(2,0) band.

Because the camera will be equipped with an optical filter and the detector will have a wavelength dependent QE, the received radiation will be lower than the average radiation. The convolution of the normalized values for different bands and the bandpass filter from fig.3.6, is illustrated in fig.3.8.

The total intensity of a band that the detector receives is the sum of the intensities for the filter response multiplied with the QE and the average intensity. This is given as

$$I_{tot} = QE \langle OH \rangle \sum (F * I)(n) \quad (3.12)$$

The average intensities of the different bands can be calculated based on the average intensities of the OH(3,1) band. The ratio of the average intensity of the (2,0) and (3,0) should equal the ratio of the total relative intensities for each.

$$\frac{\langle OH(2,0) \rangle}{\langle OH(3,0) \rangle} = \frac{\sum I'(n)_{2,0}}{\sum I'(n)_{3,1}} \approx 0.45 \quad (3.13)$$

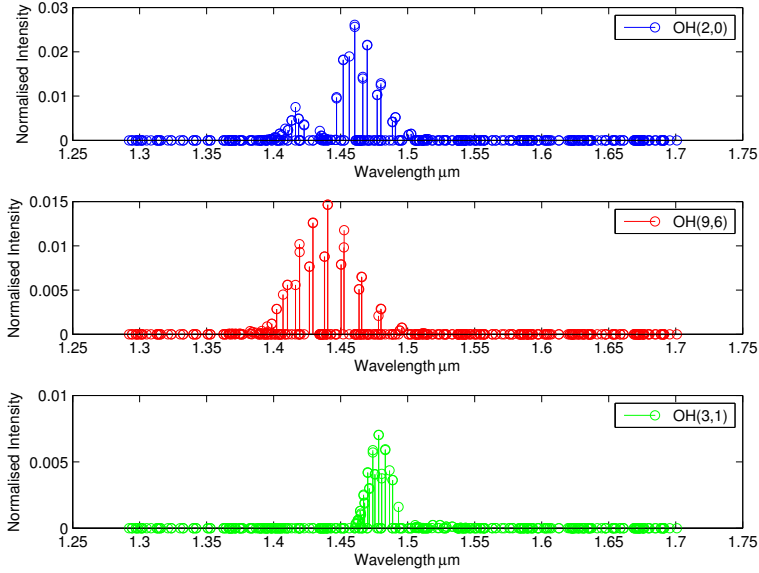


Figure 3.8: Filter response for normalized intensities.

Based on results in [23], the average intensity of the OH(3,1) at Rothera (68°S , 68°W) is

$$\langle OH(3,1) \rangle = 17.13 \text{ kR} \quad (3.14)$$

Combining eq.(3.13) and (3.14) gives

$$\langle OH(2,0) \rangle = 0.45 \cdot 17.13 \text{ kR} = 7.71 \text{ kR} \quad (3.15)$$

A similar calculation will provide the average value of (9,6),

$$\langle OH(9,6) \rangle = 0.021 \cdot 17.13 \text{ kR} = 0.35 \text{ kR} \quad (3.16)$$

Table 3.3 provides the values of the total intensities for the bands and the total intensity received at the detector for a $\text{QE} = 80\%$.

OH(2,0)	OH(9,6)	OH(3,1)	OH _{tot}
2.169 kR	0.064 kR	1.366 kR	3.599 kR

3.3 Signal to Noise Results

3.3.1 Ideal Case Camera

The SNR calculation is composed of several parameters that will change depending on the combination of the camera and lens. To make the calculations, and interpretation of the results easier, an ideal camera will be constructed. This will provide guideline for which camera to buy and what results to expect. The parameters of the ideal camera are listed in table 3.4. These parameters are based on different cameras and are all realistic. The integration time is set to a time that will contribute to a good SNR, but at the same time avoid severe blurring of the expected wave pattern.

Table 3.4: Ideal Camera

Sensor type	InGaAS
Resolution	320×320
Pixel pitch	30 μm x 30 μm
Spectral response	0.9-1.7 μm
Quantum efficiency	0.80
Integration time	3 s
Power consumption	≤ 5 W
Power supply	12 V
Digital output	14 bit
Operating temperature	-20 $^{\circ}\text{C}$ to 20 $^{\circ}\text{C}$
Lens	16 mm/ F=1.4

In order to do realistic calculations, the values of different noise sources have to be predicted. The predictions are summarized in table 3.5, where the dark current is obtained from [9], and the read noise is obtained from [3].

Table 3.5: Noise Parameters

$D(\frac{\text{electrons}}{\text{pixel}-\text{seconds}})$	$N_r(\frac{\text{electron rms}}{\text{pixel}})$
10000	65

3.3.2 Radiometric Results

The number of photons hitting the detector is given by

$$n_{DETECTOR} = \int_{\lambda_1}^{\lambda_2} \frac{\pi}{4} \frac{L_q(\lambda)A_D}{F^2(1 + M_{OPTICS}^2)} T_{OPTICS}(\lambda)T_{ATM}(\lambda)t_{int}d\lambda \quad (3.17)$$

From this, one can see that by setting

$$T_{OPTICS} = 1$$

$$T_{ATM} = 1$$

and independent of λ , the only factor dependent on the wavelength will be the spectral photon radiance L_q . The photon radiance can be calculated by combining eq.(2.29), and the total intensity from table 3.3.

$$L = \int_{\lambda_1}^{\lambda_2} L_q(\lambda) d\lambda = \sum_{\lambda_1}^{\lambda_2} L_q(\lambda) = \sum_{\lambda_1}^{\lambda_2} I(\lambda) \frac{10^{10}}{4\pi} = OH_{tot} \frac{10^{10}}{4\pi} = 2.9 \cdot 10^{12} \left(\frac{\text{photons}}{\text{m}^2 \cdot \text{s} \cdot \text{sr}} \right) \quad (3.18)$$

The replacement of the integral with a sum can be justified by the discrete intensity values in the data from [18].

The optical magnification M_{OPTICS} in eq.(3.17) is given as the ratio between the distance from the detector to the entrance aperture, and the distance from the entrance aperture to the source, as indicated by figure 3.9. Because of the height of the satellite, this value will equal zero. The radiometric results for the ideal camera are listed in table 3.6

$$M_{OPTICS} = \frac{R_2}{R_1} \approx 0, \text{ since } R_2 \ll R_1 \quad (3.19)$$

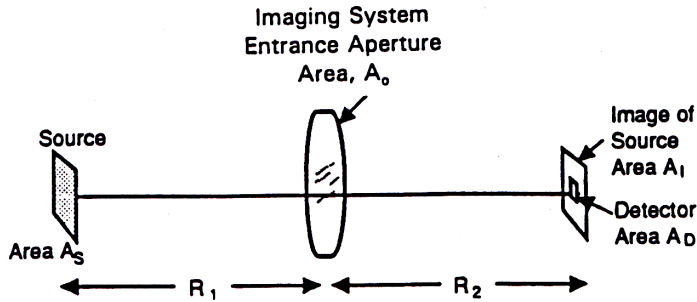


Figure 3.9: Image system from [14].

Table 3.6: Radiometric Results

$\frac{n_{DETECTOR}}{s}$	$L \left(\frac{\text{photons}}{\text{m}^2 \cdot \text{s} \cdot \text{sr}} \right)$	$A_D (\text{m}^2)$	M_{optics}	T_{OPTICS}	T_{AMT}
$8.4613 \cdot 10^7$	$2.9 \cdot 10^{12}$	$7.4 \cdot 10^{-5}$	0	1	1

3.3.3 SNR

Based on section 2.4.2, the SNR will be given by

$$\Delta SNR = \frac{\Delta P Q_e t_{int}}{(\Delta P Q_e t_{int} + D_{dark} t_{int} + N_r^2)^{\frac{1}{2}}} \quad (3.20)$$

ΔP = Difference in photon flux($\frac{photons}{pixel \cdot seconds}$)

Q_e = Quantum efficiency

t_{int} =Integration time

D_{dark} = Dark current($\frac{electrons}{pixel \cdot seconds}$)

N_r = Read noise($\frac{electrons}{pixel}$)

The difference photon flux between the wave top and bottom is given by

$$\Delta P = \frac{B \cdot \Delta n_{detector/second}}{\text{Number of pixels}} \quad (3.21)$$

where B is the binding factor, i.e. the number of pixels that are combined in to a single pixel, e.g. a 2x2 pixel combination will give a binding factor of B = 4. This will increase the GSD by a factor of $\frac{B}{2}$ (quadratic binding), and increase the dark current as $D_{dark} = B \cdot D$. The maximum amount of binding is limited by the Nyquist freq. and is given by

$$\frac{B_{max}}{2} \cdot GSD \leq \frac{\lambda_{GW}}{2} \quad (3.22)$$

$$B_{max} \leq \frac{13 \text{ km}}{GSD} = \frac{13 \text{ km} \cdot f}{p \cdot H} \quad (3.23)$$

Figure 3.10 illustrates the maximum binding factor for the ideal camera at a height of H = 650 km. Increasing the amount of binding is the same as decreasing the resolution. In order to have easy detection of the wave pattern, the binding factor should always be lower than maximum value. Note that the binding of pixels will be done in quadratic patterns, so the theoretical max value may not correspond to a realistic value.

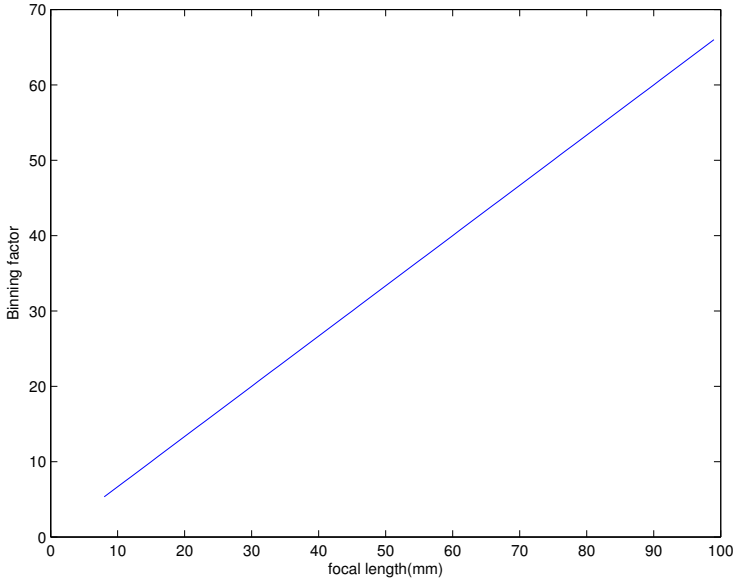


Figure 3.10: The maximum number of pixels to bind vs. focal length at a height of 650 km

For the camera in table 3.4, with a binding factor of $B = 4$ (resolution of 160×128), the photon flux difference between a wave top and bottom can be expected to be

$$\Delta P = \frac{4 \cdot 8.4613 \cdot 10^7}{320 \times 256} = 4.1 \cdot 10^3 \left(\frac{\text{photons}}{\text{pixel} - \text{seconds}} \right) \quad (3.24)$$

The SNR for a single images from the ideal camera is plotted in figure 3.11. The figure indicate that an integration time of three seconds is not sufficient to give a SNR larger than the minimum requirement of $\text{SNR} \geq 2$. The choice of an integration time of max three seconds is justified in section 3.4.1, and is connected to wavelength of the waves to be observed. From figure 3.10 binding factor can be increased to the maximum value of $B = 9$, but this will provide the lowest resolution.

Another way of increasing the SNR is to average several images. From [11], the averaging of images reduces the variance of the noise by a factor of N , where N is the number of average images. The average variance of the noise is given as

$$\sigma_{avg.n}^2 = \frac{\sigma_n^2}{N} \quad (3.25)$$

The SNR for the final image will then be

$$\Delta\text{SNR}_{average} = \frac{\Delta s_{target}}{\sigma_{avg.n}} = \sqrt{N} \cdot \Delta\text{SNR} \quad (3.26)$$

where ΔSNR is the SNR for one image. Figure 3.12 illustrates the amount of images that have to be averaged in order to provide a certain SNR. The increase in SNR will only apply to the area of the images that overlap with each other, and to achieve this, motion compensation is necessary. Because of the overlap, the FOV will decrease.

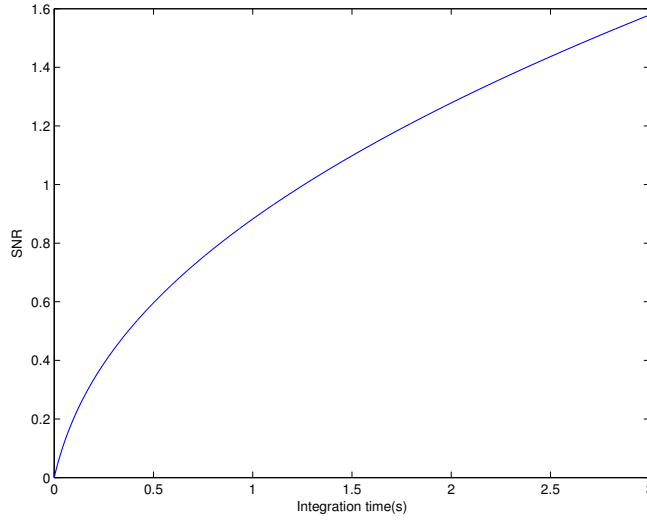


Figure 3.11: SNR for a single image from the ideal camera.

3.4 Image/Data Acquisition

3.4.1 Motion Blur

In this thesis, motion blur will be treated as a measure in the amount of pixels per second an image will move. Because of the satellites velocity of approximately 8 km/s , and an integration time of several seconds, one can expect that motion blur will occur. The speed of the satellite will have to be converted to the speed of an image, and the blur can be calculated based on the integration time. The speed of the satellite is given by

$$V_{Sat.OH} = \frac{2\pi \cdot R_{OH}}{T_{sat}} \approx 7.5 \frac{\text{km}}{\text{s}} \quad (3.27)$$

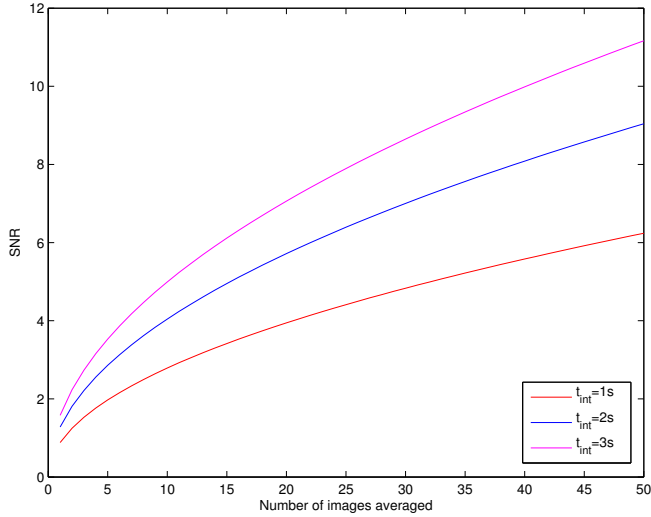


Figure 3.12: Signal to noise for a number of images.

The speed of an image will be

$$V_{pix} = \frac{V_{Sat.OH}}{GSD} \left(\frac{pixler}{s} \right) \quad (3.28)$$

for the ideal case camera with a binding factor of $B = 4$, the speed will become

$$V_{pix} = \frac{7.5}{\frac{4}{2} \cdot 1} \approx 3.75 \left(\frac{pixler}{s} \right) \quad (3.29)$$

The number of pixels an image will move during the integration time is

$$d_{pix} = V_{pix} \cdot t_{int} \quad (3.30)$$

The time it would take for the image to move one pixel and get a blur is $t_{int} \approx 0.26$ s. In this calculation, the integration time would include any potential time the camera may use to reset/get ready to take another image.

In [11], the effects of blur on spatial frequencies are shown. Figure 3.13 illustrates the degradation function. The zeros indicate which spatial frequency that will be wiped out by motion blur. Based on [22], the expected average wavelength of gravity waves the satellite will observe is $\lambda_{avg} = 26$ km, and this will correspond to a spatial frequency of $f_{avg} \approx 11$ (cycles/image). The system should be design in a manner that these frequencies avoid blurring. In this case, choosing an integration

time of one second provides the possibility to observe short wavelengths without blur, but a longer integration time will provide a better SNR. Note that the spatial frequencies that can be observed is also limited by resolution. For the ideal camera, this should correspond to a max spatial freq. of ≈ 80 cycles/image.

In figure 3.13, the first zero occur at a frequency of 20 cycles/image, and will correspond to a wave with a wavelength of $\lambda = 15$ km. By choosing the integration time to be $t_{int} = 3$ s, wavelengths at 15 km and lower will experience blur. Assuming possibility to change the integration time in orbit, the SNR calculation should be done with $t_{int} = 3$ s. From figure 2.5, it is clear that the choice of this integration time will contribute to losing a small amount of waves, at the cost of an increased SNR. The highest spatial frequency that can be observed is limited by the resolution.

It is important to notice that the result in this section is based on horizontal blur, and represent blur in the direction of the satellite. If the waves are propagating with a phase speed in a perpendicular direction to the satellite orbit (polar), i.e. the waves are propagating east/west, the wavelengths will not be affected by this blur. The blur considered in this section is not the only blur that can affect the image. Blur introduced by the rotation of satellite have not been considered in this thesis, but should be looked into in future work.

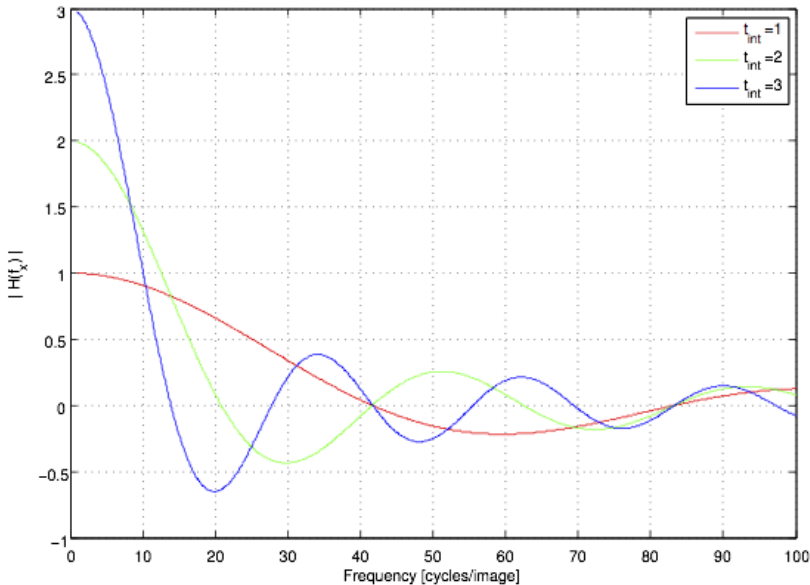


Figure 3.13: Image degradation function. The zeroes describes which spatial frequencies that are totally blurred out [11].

3.4.2 Motion Compensation

In the process of averaging several images into one, it is useful to calculate the effective FOV of the final image, i.e the size of the area it will image. This will be given by how well the last image overlap with the first one. The overlap factor will describe how many pixels of a given image will correspond to the first, and is given as

$$O_{overlap} = \frac{N_{pix} - V_{pix} \cdot \Delta t}{N_{pix}} = 1 - \frac{V_{pix} \cdot I_N}{N_{pix} \cdot fps} \quad (3.31)$$

where I_N is the number of images after the first, and fps is the frame rate in (Hz). The effective field of view of the final image is given as

$$FOV_{effective} = O_{overlap} \cdot N_{pix} \cdot GSD \quad (3.32)$$

where N_{pix} describe the number of pixels in e.g the x-direction of the detector. Figure 3.14 describe the visual ground segment of the final image.

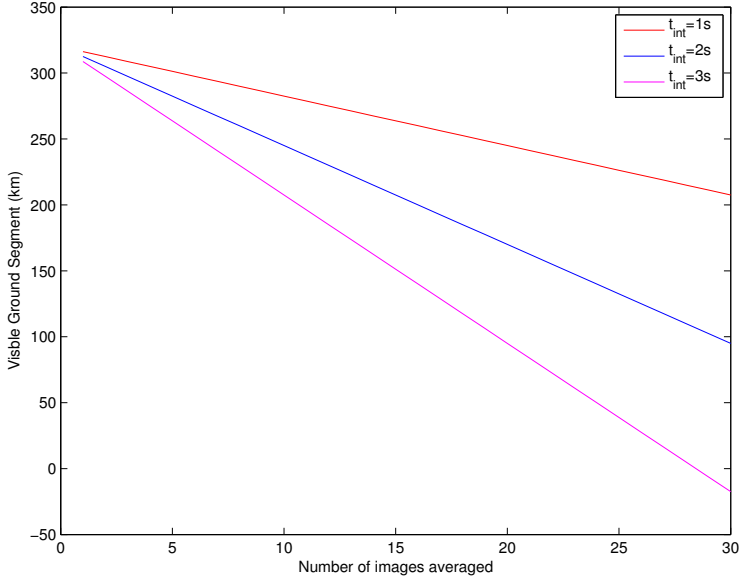


Figure 3.14: Illustration of the size of the area the detector can image based on integration time and number of images averaged.

3.4.3 Observing phase speed

Since both the satellite and gravity waves are moving, figure 3.15, there could be a possibility to detect wave moments. The time it would take for the satellite to move from one FOV to a completely new one, i.e. the time it would take to get no overlap between the first and last image, is given by

$$T_{image} = \frac{N_{pix}}{V_{pix}} = \frac{160}{3.75} \text{ s} \approx 43 \text{ s} \quad (3.33)$$

From figure 2.5, it is shown that the observed phase speeds have a range from ≈ 10 to 100 m/s. The typical values of the phase speed have a range of 30-60 m/s, and the average value is ≈ 48 m/s [22]. The observed phase speed is defined as $c = c_i + u$, where c_i is the intrinsic phase speed of the waves and u is the background wind in the direction of the wave propagation. To calculate the intrinsic phase speed require knowledge of the local wind speeds. This will only be possible if the satellite take images over location where wind data can be obtained.

Based on the eq.(3.33) the speed a wave would need to have in order to move during the time of one image/FOV is given as

$$V_w = \frac{GSD}{T_{image}} = \frac{2 \text{ km}}{43 \text{ s}} \approx 47 \text{ (m/s)} \quad (3.34)$$

This will be the phase speed required to move one pixel during the time the satellite will cover an area of ≈ 300 km. If the max phase speed of a wave is 100 m/s, it would correspond to a movement just over two pixels. Detecting so small movement could be hard, if not impossible, and would require a technique that would compare several averaged images for the same area. Decreasing the binning factor will decrease the speed necessary to move one pixel and make detection easier. This would on the other hand be the same as "sacrificing" the SNR in order to maybe detect movement, and since the main goal is to detect wavelengths, the SNR will have a higher priority than the phase speed. From this it can be concluded that wave movement and phase speeds will not be detected by the camera.

3.5 Summary

This section will summarize the most important results presented in this chapter. Table 3.7 present different camera requirements. In order to obtain scientific data of any value, these requirements have to fulfilled. Table 3.8 presents the results from the ideal camera from table 3.4. Based on these values, it can be concluded that with the right camera, the NUTS have the possibility to detect wavelengths, intensity and orientation of atmospheric gravity waves. Due to the high speed

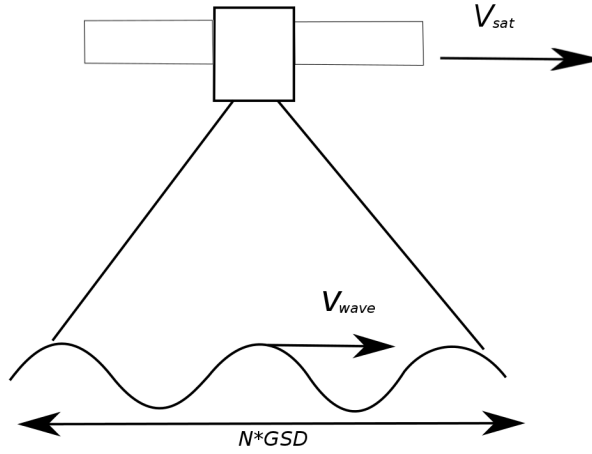


Figure 3.15: Because of the high speed of the satellite compared to the phase speed of gravity waves, detection of wave movement will be difficult.

of the satellite compared to gravity waves, the detection of phase speeds will be impossible.

Table 3.7: Camera Requirements

Parameter	Requirement
Focal length	$> 1.4 \text{ mm}$
GSD	$\leq 13 \text{ km}$
FOV	$< 97^\circ$
Operating temperature	$-20^\circ \text{ to } 20^\circ$
Size dimension	$\leq 92 \times 88 \times 65 \text{ mm}^3$
Max lens diameter	35 mm

Table 3.8: Ideal Camera Results

Parameter	Result
Focal length	16 mm
F-number	1.4
GSD	2 km
Resolution	160×160
Binning factor	4
B_{max}	13
FOV	34°
Ground segment one image	320 km
Blurred wavelengths	≤15 km
Integration time	3 s
Δ SNR for one image	1.6
Effective FOV	200 km
N_{images}	11
Δ SNR _{average}	5.5

Chapter 4

Discussion and Future Work

An educational satellite project based on projects reports and masters theses from a high number of students from several disciplines is an ever changing project. Because of this, some of the results presented in this thesis are based on analyzes where the parameters might suddenly change. The changes may come from other and more important subsystems that will affect the payload in some way, or it could be changes based on external factors like economics. Because of this, some of the results in this thesis may be viewed as guidelines instead of final results. In this chapter different camera alternatives and noise sources and future work will be discussed. At the end, the most suitable camera with the expected results are presented.

4.1 Camera Alternatives

From the results and analysis in chapter 3, several camera alternatives have been found. In the process of limiting the search, factors like size, weight and power consumption have been prioritized. To find a camera without cooling and a good temperature range is emphasized and have been a challenge. The reason to look for cameras without cooling is the limited effect it will have in space, and the high power consumption. Some of the cameras are delivered with thermoelectric coolers that will work in zero g environment [5], but it would have to consume a small amount of power.

The camera alternatives have been narrowed down to two different camera manufacturers: Xenics and Raptor Photonics. Both of these are European, so ITAR regulations are avoided. The cameras are listed in Table 4.1. The data sheets for the individual cameras can be found in the appendix. The price for only one of

the cameras are listed. This is unfortunate since the cost of a camera could be the most limiting factor.

Table 4.1: Camera Alternatives

Manufacturer	Camera	Price (EUR)
Xenics	Bobcat-640-GigE	23 600
Raptor	OWL SW1.7HS	-
Raptor	OWL 1.7-CL-320	-
Raptor	OWL SW1.7 CL-640	-

Xenics Bobcat-640-GigE

The most important parameters of the Xenics Bobcat are listed in table 4.2. The advantages of this camera are many. The detector, power consumption and power supply are well suited for this project. The optical interface with C-mount will also make it possible to fit different lenses to the camera. The challenge will then be to find a lens that with a maximum diameter of 35 mm and a maximum length of 33.6 mm. It is also important to keep in mind that the f-number must be as low as possible. The operational temperature range is well within the requirements for the satellite. Since resolution is higher than required, a binning of the pixels will be necessary. The camera comes with thermoelectric cooling, and the effect of it should be tested. The data sheet do not include information about the dark current, and since the detector will be dark noise limited [9], it is important to get this data in the future. The frame rate will correspond to an integration time 8.3 ms. This is far below the ideal integration time of three seconds. If this can not be change, a higher number of images must be averaged. This will affect the data acquisition part of the payload, i.e the data bus, memory and FPGA. The interface of the camera is GigE Vision. This interface is unknown to the NUTS team, so further investigation is necessary. There is also no data how this camera would respond to mechanical test it would face.

4.1.1 OWL

The Rapotor photonics cameras have a lot of common parameters and the important ones are listed in table 4.3. From this table one can see that the camera is to large for the payload area. The reason this camera should still be considered is based on the fact that $\approx 70\%$ of the cameras they sell are modified to suit the customers use, and they have previous experience with delivering cameras for space missions (JAXA) [2]. If the cameras can be made smaller, they are a good alternative. The CL-640 and CL-320 can both deliver integrations time of one second, and the interface is CameraLink.

Table 4.2: Xenics Bobcat-640-GigE

Sensor type	InGaAS
Resolution	640×512
Pixel pitch	20 μm x 20 μm
Spectral response	0.9-1.7 μm
Quantum efficiency	0.90
Frame rate _{max}	120 Hz
Power consumption	4 W
Power supply	12 V
Digital output	14 bit
Operating temperature	-40 °C to 70 °C
Weight (lens not included)	≤ 150 g
Size dimensions	40 × 40 × 40 mm ³

Table 4.3: Common Parameters for OWL

Spectral response	0.9-1.7 μm
Quantum efficiency	≈ 0.80
Power consumption	≤ 5 W without TEC
Power supply	12 V
Digital output	14 bit
Operating temperature	-20 °C to 55 °C
Weight (lens not included)	≤ 282 g
Size dimensions	50 × 50 × 82 mm ³

4.2 Camera Conclusion

Both Xenics and Raptor photonics offer custom designed cameras, and a list of the NUTS specifications have been sent to sales personal that represent each manufacturer. The list and contact information can be found in the appendix. At the time of December 2012 there have been no response to the list of specifications. Based on the previous section it is therefore recommended that NUTS project choose the Xenics Bobcat-640-GigE. This camera lacks information about the dark current and it is unknown if the interface will work on the satellite. Should a different camera alternative arise in the future, it is my hope that this thesis will provide the necessary information to make sure the right camera is selected.

The expected results of the Xenics Bobcat-640-GigE is summarized in table 4.5. In order to achieve a $\text{SNR} \geq 2$ with an integration time of $t_{int} = 3$, the minimum amount of images that has to be averaged are 11. This will correspond to an area on the airglow layer of 579×115 km (Overlap of $\approx 30\%$). It is important to note that the orientation of the camera will affect the number of averaged imaged that is needed in order to produce a $\text{SNR} \geq 2$. In this calculation the smallest FOV have been orientated in the north/south direction. The disadvantage of this orientation is that the effective FOV will be smaller compared to having the largest FOV in the north south direction. Note that because of the quadratic binning, not all of the pixels on the detector are utilized.

Table 4.4: Xenics Bobcat-640-GigE

Parameter	Result
Focal length	16 mm
F-number	1.4
GSD	2.25 km
Resolution	213×170
Binning factor	9
B_{max}	17
FOV	46° and 37°
Ground segment one image	479 km and 383 km
Blurred wavelengths	≤ 15 km
Integration time	3 s
ΔSNR for one image	0.6
Effective FOV	479 km and 115 km
N_{images}	12
$\Delta \text{SNR}_{average}$	2

4.3 Noise

4.3.1 Dark Current

The InGaAs sensor will most likely be dark noise limited [9], and since there is no data on the dark current in the Xenics Bobcat-640-GigE, it is assumed that it will be the same as the for the ideal camera ???. In the future, there should be an investigation on the effect the dark current will have on the SNR. There should also be a study on the heat distribution in the satellite. It is important that the detector of the camera is kept as cool as possible.

4.3.2 Detector

The detector will have different kinds of noises that will include fixed pattern noise, detector offset and hot pixels. Techniques to get rid of fixed pattern noise and detector offset is presented in [11]. Hot pixels are pixels which look brighter than they should, and this is caused by electric charge that leaks into the pixel well. In the process of binning the pixels on the detector, have to average the values of the relevant pixels, and a hot pixels will make the resulting pixel look brighter than it should. This can be avoided by identifying hot pixels preflight. In orbit, the satellite should send down a RAW image taken with the shutter closed. This will identify the noise in the detector and image processing could be used to get rid of it.

4.3.3 Other Noise Sources

The camera might be affected by undesired radiation from auroras. This strength of this radiation will be $\approx 25\%$ to that of the airglow at $\approx 1.45 \mu\text{m}$???. Areas with low humidity might also contribute to noise, but this is highly unlikely since these areas have few noise sources (cities etc.).

4.4 Data Processing

A lot of work has to be done on this topic in the future. The main objective would be to figure out how to control the camera and how to store the images. The wiring of the system should be something like this:

$$CAMERA < - > FPGA < - > FLASH < - > MCU$$

The microcontroller (MCU) onboard the satellite will be an AVR UC3 32 bit. The aim will be to make an interface with the help of a FPGA in order to control the camera and to transfer images from the camera to a flash memory. In addition to

this, there must be a system that can do motion compensation, averaging of the images, noise removal and compression. In the future there should be done a study to find out what SNR value would be required for a compression algorithm.

4.5 Power Consumption

The power consumption of the camera is an important parameter in the satellite design. The satellite will run on batteries that will be recharged by solar panels. Since the camera will only be active during the dark side of the orbit, it would have to depend solely on the power from the batteries. The payload will not be the only system active during that time, so the amount of power available will be limited. The power supply of the backplane in the satellite was originally intended to deliver a voltage of 3.3 V and 5 V. This was a severe limitation in the search for an appropriate camera. During this search, the need for a higher voltage emerged. It was determined to design the backplane to deliver a voltage of 12 V. At the time of this thesis, a power budget for the total satellite was not in place. Since the payload is not a important system for keeping the satellite alive, the amount of power dedicated to it should be based on what is left after the essential systems have been prioritized. In the search for a camera, it was assumed that the satellite was equipped with a battery providing 30 Wh.

4.6 Camera Conclusion

Both Xenics and Raptor photonics offer custom design for their cameras, a list of the NUTS specifications have been sent to sales personal that represent each manufacturer. The list and contact information can be found in the appendix. At the time of December 2012 there have been no response to the list of specifications. Based on the previous section it is therefore recommended that NUTS project choose the Xenics Bobcat-640-GigE.

The expected results of this camera is summarized in table 4.5. In order to achieve an $\text{SNR} \geq 2$ with an integration time of $t_{int} = 3$, the minimum amount of images that have to be averaged are 11. This will correspond to an area on the airglow of 579×115 km (Overlap of $\approx 30\%$). It is important to note that the orientation of the camera will affect the number of averaged imaged that will be needed in order to produce a $\text{SNR} \geq 2$. In this calculation the smallest FOV have been orientated in the north/south direction. The disadvantage of this orientation is that the effective FOV will be smaller compared to having the largest FOV in the north south direction. Because of the quadratic binning, not all of the pixels on the detector are utilized.

Table 4.5: Xenics Bobcat-640-GigE

Parameter	Result
Focal length	16 mm
F-number	1.4
GSD	2.25 km
Resolution	213×170
Binning factor	9
B_{max}	17
FOV	46° and 37°
Ground segment one image	479 km and 383 km
Blurred wavelengths	≤15 km
Integration time	3 s
Δ SNR for one image	0.6
Effective FOV	479 km and 115 km
N_{images}	12
Δ SNR _{average}	2

4.7 Conclusion

Finding a suitable camera for the CubeSat platform has been a challenging task. The complexity of the problem arises from the many dependencies and a large amount of tradeoffs. There is also many unknown factors attached to this project. Hopefully this thesis will provide a good introduction to the science behind the goal of imaging gravity waves, and provide either an answer, or a guideline to the best suited camera for the NTNU test satellite.

Chapter 5

Appendix

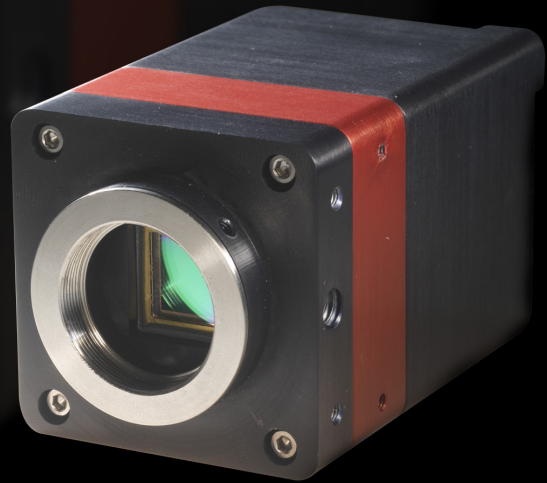
Sales person from Xenics: lena.chytraeus@parameter.se

Sales person from Raptor Photonics: magnus.larsson@penlink.se

OWL SW1.7CL 320

Rugged, high sensitivity, digital SWIR camera

Preliminary



Key Features and Benefits

SWIR technology with Optional Visible Extension

- **14 bit CameraLink output.**
Enables high speed digital video with intelligent auto AGC
- **On-board Automated Gain Control (AGC).**
Enables clear video in all light conditions
- **On-board intelligent 3 point NUC.**
Enables highest quality images
- **Ultra compact, Low power (< 5W).**
Ideal for hand-held, mobile or airborne systems
- **Rugged, No fan.**
Enables integration into UAV, handheld or any Electro-Optic system

Resolution	320 x 256
Frame Rate	25/30/50/60 Hz
CameraLink	14 bit
Wavelength Range	VIS-SWIR

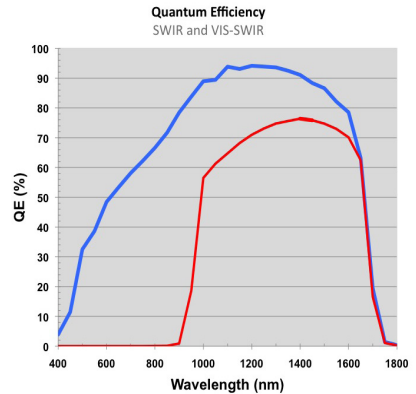


● ● ● ● ● ● ● ● ● ● Capturing Tomorrow

Specification for OWL SW1.7 CL-320

FPA Specification	
Sensor	Alcatel-Thales III-V Lab
Sensor Type	InGaAs PIN-Photodiode
Active Pixel	320 x 256
Pixel Pitch	30µm x 30µm
Active Area	9.6mm x 7.68mm
Spectral response ¹	0.9µm to 1.7µm or 0.4µm to 1.7µm
Noise (RMS)	<150 electrons
Quantum Efficiency	>70% @ 1.5µm
Pixel Operability	>99%
Camera Specification	
Digital Output Format	14 bit CameraLink (Base Configuration)
Exposure time	500ns to 1 / frame rate
Shutter mode	Global shutter
Frame Rate	25Hz, 30Hz, 50Hz or 60Hz
Optical Interface	C mount (selection of SWIR lens available)
Camera Setup / Control	CameraLink
Dynamic Range	14 bit
Trigger interface	Trigger IN and OUT - TTL compatible
Power supply	12V DC ±10%
TE Cooling	ON / OFF
Image Correction	3 point NUC (offset, Gain & Dark Current) + pixel correction
Functions controlled by serial communication	Exposure, intelligent AGC, Non Uniformity Correction, Gamma, Pk/Av, TEC, ROI
Camera Power Consumption ²	< 5W without TEC
Operating Case Temperature ³	-20°C to +55°C
Storage Temperature	-30°C to +60°C
Dimensions & Weight	50mm x 50mm x 82mm / 282g

Quantum Efficiency



Sample Applications

- 860, 1064 & 1550nm laser line detection
- Active Imaging
- Airborne Payload
- Hand Held Goggles
- Imaging through fog
- Range finding
- Vision enhancement
- Semiconductor Inspection
- Solar Cell Inspection
- Telecommunications
- Thermography
- Astronomy
- Telecommunications

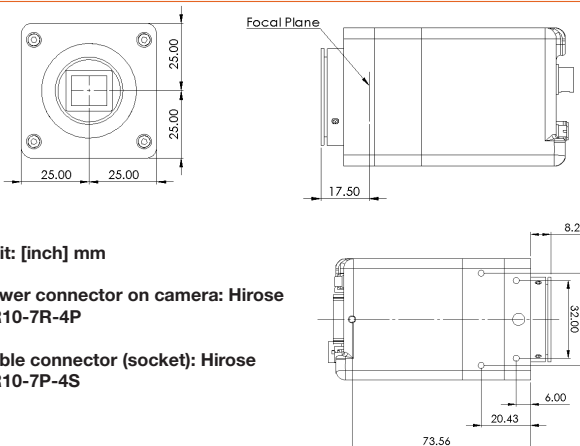
Raptor Photonics Limited reserves the right to change this document at any time without notice and disclaims liability for editorial, pictorial or typographical errors.

Note 1: Optional filters available: Low, High or bandpass

Note 2: Additional up to 5W with TEC switched on

Note 3: Extended Operating Temperature range on request

Dimensions



Unit: [inch] mm

Power connector on camera: Hirose
HR10-7R-4P

Cable connector (socket): Hirose
HR10-7P-4S

Document #: OWL1.7-CL-320 0912PR1

Ordering Information

Camera

OWL SWIR digital camera OW1.7-CL-320

OWL Power Supply Cable RPL-HR4-K

Optional Accessories

Epix base CL card RPL-EPIX-EB1

Epix base notebook CL card RPL-EPIX-ECB1-54

Epix Xcap ltd software RPL-XCAP-LTD

CameraLink Cable, 2m⁴ RPL-CL-CBL-2M

Optical SWIR lenses⁵ RPL-xx-xxxx

Note 4: Longer CL cable available

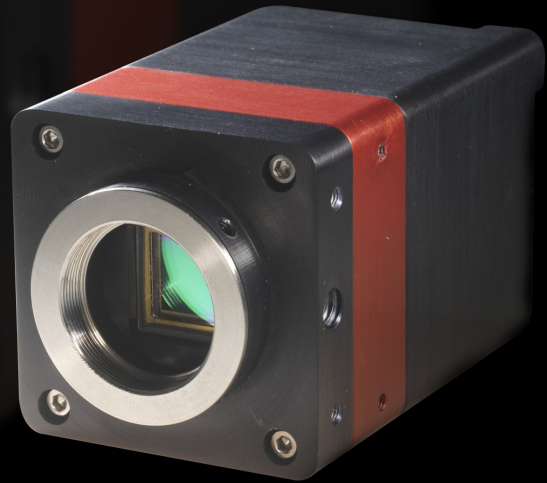
Note 5: Please consult us to check our range of lenses

Equipment may require UK Government authorisation for export purposes

OWL SW1.7CL 640

Rugged, high sensitivity, digital VIS-SWIR camera

Preliminary



Key Features and Benefits

The best performing SWIR camera in the World!

- **VIS-SWIR technology.**
Enables high sensitivity imaging from 0.4mm to 1.7mm
- **15µm x 15µm pixel pitch.**
Enables highest resolution VIS-SWIR image
- **< 65 electrons readout noise.**
Enables highest VIS-SWIR detection limit
- **14 bit CameraLink output.**
Enables high speed digital video with intelligent auto AGC
- **On-board Automated Gain Control (AGC).**
Enables clear video in all light conditions
- **On-board intelligent 3 point NUC.**
Enables highest quality images
- **Ultra compact, Low power (< 5W).**
Ideal for hand-held, mobile or airborne systems
- **Rugged, No fan.**
Enables integration into UAV, handheld or any Electro-Optic system

Resolution	640 x 512
Frame Rate	10 to 120Hz
CameraLink	14 bit
Wavelength Range	VIS-SWIR



● ● ● ● ● ● ● ● ● ● Capturing Tomorrow

Specification for OWL SW1.7 CL-640

FPA Specification	
Sensor	SCD
Sensor Type	InGaAs PIN-Photodiode
Active Pixel	640 x 512
Pixel Pitch	15µm x 15µm
Active Area	9.6mm x 7.68mm
Spectral response ¹	0.4µm to 1.7µm
Noise (RMS)	<195 electrons Low Gain <65 electrons High Gain
Quantum Efficiency	>73% @ 1.064µm, 78% @ 1.55µm
Pixel Well Depth	700Ke Low Gain 15Ke High Gain
Pixel Operability	>99.5%
Camera Specification	
Digital Output Format	14 bit CameraLink (Base Configuration)
Exposure time	500ns to 1 / frame rate
Shutter mode	Global shutter
Frame Rate	10Hz to 120Hz programmable, 25ns resolution
Optical Interface	C mount (selection of SWIR lens available)
Camera Setup / Control	CameraLink
Dynamic Range	14 bit
Trigger interface	Trigger IN and OUT - TTL compatible
Power supply	12V DC ±10%
TE Cooling	ON / OFF
Image Correction	3 point NUC (offset, Gain & Dark Current) + pixel correction
Functions controlled by serial communication	Exposure, intelligent AGC, Non Uniformity Correction, Gamma, Pk/Av, TEC, ROI
Camera Power Consumption ²	< 5W without TEC
Operating Case Temperature ³	-20°C to +55°C
Storage Temperature	-30°C to +60°C
Dimensions & Weight	50mm x 50mm x 82mm / 282g

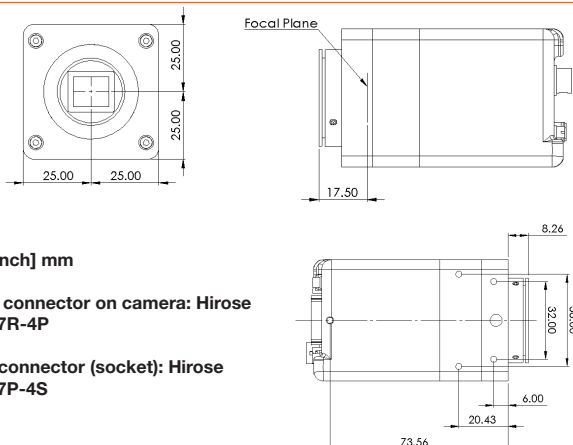
Raptor Photonics Limited reserves the right to change this document at any time without notice and disclaims liability for editorial, pictorial or typographical errors.

Note 1: Optional filters available: Low, High or bandpass

Note 2: Additional up to 5W with TEC switched on

Note 3: Extended Operating Temperature range on request

Dimensions



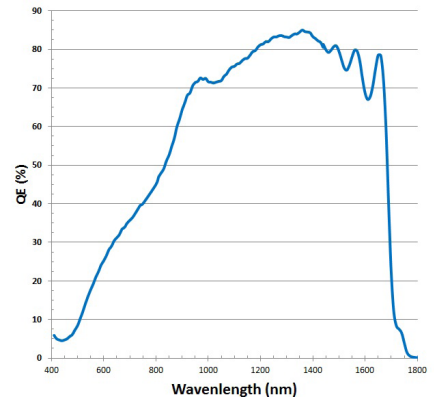
Unit: [inch] mm

Power connector on camera: Hirose
HR10-7R-4P

Cable connector (socket): Hirose
HR10-7P-4S

Document #: OWL1.7-CL-640 0912PR1

Quantum Efficiency



Sample Applications

- 860, 1064 & 1550nm laser line detection
- Active Imaging
- Astronomy
- Airborne Payload
- Hand Held Goggles
- Imaging through fog
- Range finding
- Semiconductor Inspection
- Solar Cell Inspection
- Telecommunications
- Thermography
- Telecommunications
- Vision enhancement

Ordering Information

Camera

OWL SWIR digital camera OW1.7-CL-640

OWL Power Supply Cable RPL-HR4-K

Optional Accessories

Epix base CL card RPL-EPIX-EB1

Epix base notebook CL card RPL-EPIX-ECB1-54

Epix Xcap ltd software RPL-XCAP-LTD

CameraLink Cable, 2m⁴ RPL-CL-CBL-2M

Optical SWIR lenses⁵ RPL-xx-xxxx

Note 4: Longer CL cable available

Note 5: Please consult us to check our range of lenses

Equipment may require UK Government authorisation for export purposes

Imagine the invisible

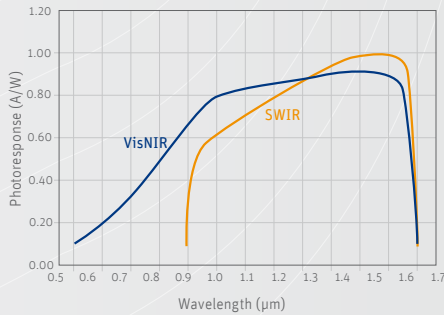
Scientific

Bobcat-640-GigE

High resolution small form factor InGaAs camera



Low noise and dark current with fast data transfer over GigE Vision



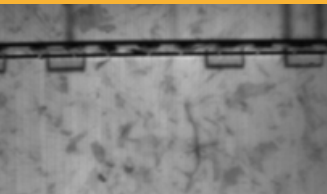
With superior image quality the Bobcat-640-GigE is available as a complete digital infrared camera system with on-board image processing.

The Bobcat-640-GigE comes with an industry-standard GigE Vision interface which makes it much easier to integrate in your own set-up.

With the Bobcat-640-GigE SWIR camera you can look through glass, so standard available C-Mount lenses and protective camera housings can be used. Again making this camera affordable for a wide variety of scientific applications.

The Thermo Electric (TE) stabilization reduces dark current and optimizes the noise performance.

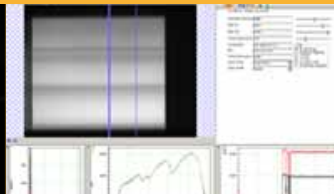
Designed for use in



☛ Solar cell inspection



☛ Stress analysis



☛ R&D SWIR



☛ Laser beam profiling

Applications

- R&D (SWIR) range
- Solar cell inspection
- Laser beam profiling
- Hyperspectral imaging
- Thermal imaging of hot objects (300°C to 800°C range)

Benefits & Features

- Small form factor
- Small GigE interface
- On-board image processing
- High Operating Temperature
- High sensitivity and excellent image quality
- Flexible programming in an open architecture

Broad range of accessories available to simplify your inspection

↳ Lens & filter options



↳ Inputs



↳ Software



- Xeneth advanced
- Xeneth SDK

↳ Outputs

↳ Specifications

Array specifications	Bobcat-640-GigE
Array type	InGaAs
Spectral band	0.9 μm to 1.7 μm Optional 0.4 μm to 1.7 μm
# Pixels	640 x 512
Pixel pitch	20 μm
Array cooling	TE1 cooled
Gain setting	CTIA: High & Low Gain
Pixel operability	> 99%

Camera Specifications	Bobcat-640-GigE
Lens (included)	
Focal length	25 mm
Optical interface	C-mount (Broad selection of lenses available)
Imaging performance	
Frame rate	120 Hz
Window of interest	Minimum size 4 x 1
Integration type	Snapshot
Readout mode	ITR
Onboard image processing	Configurable single NUC Auto level and span control CLAHE: Contrast Limited Adaptation Histogram Equalization
A to D conversion resolution	14 bit
Interfaces	
Camera control	GigE Vision
Image acquisition	GigE Vision
Trigger	Trigger In or Out
Power requirements	
Power consumption	4 W
Power supply	12 V
Physical characteristics	
Ambient operating temperature	-40°C to 70°C
Dimensions	40 W x 40 H x 40 L mm ³
Weight camera head	< 150 g (lens not included)

↳ Product selector guide

Part number	Interface	Frame rate	VisNIR
XEN-000296	GigE Vision	100	No
XEN-000099			Yes

Bibliography

- [1] Thermal vacuum testing of hincube. Technical report, -, -.
- [2] Magnus larsson, product manager, penlin ab.
- [3] Owl sw1.7hs infrared camera from raptor photonics (data sheet).
- [4] http://chemwiki.ucdavis.edu/@api/deki/files/13247/=Normal_modes_water.png.
- [5] http://spinoff.nasa.gov/Spinoff2009/ip_4.html.
- [6] <http://web.nmsu.edu/~snsm/classes/chem435/Lab9/>. -.
- [7] http://www.rocketrange.no/?page_id=254.
- [8] <http://www.sensorsinc.com/GaAs.html>.
- [9] Introduction to scientific ingaas fpa cameras. Technical report, Princeton Instruments, 2012.
- [10] David G. Andrews. *An Introduction to Atmospheric Physics*. Cambridge University Press, 2012.
- [11] Marianne Bakken. Signal processing for communicating gravity wave images from the ntnu test satellite. Master's thesis, NTNU, 2012.
- [12] Roger Birkeland. Statement from project manager. -, - -.
- [13] California Polytechnic State University Std. *CubeSat Design Specifications*.
- [14] Gerald C.Holst. *CCD ARRAYS CAMERAS and DISPLAY*. JCD Publishing, second edition, 1998.
- [15] Robert D.Fiete. Image quality and λ fn/p for remote sensing systems. *Optical Engineering*, 1999.

- [16] G.D. Boreman E.L. Dereniak. *Infrared Detectors and Systems*. John Wiley and Sons, 1996.
- [17] Dong L.Wu et al. Remote sounding of atmospheric gravity waves with satellite limb and nadir techniques. *Advances in Space Research*, 2006.
- [18] Mark C.Abrams et al. High resolution fourier transform spectroscopy of the meinel system of oh. *The Astrophysical Journal*, 1994.
- [19] Zhenhua Li et al. Gravity wave characteristics from oh airglow imager over maui and propagation preference due to doppler-shifting by background wind. *Journal of Geophysical Research*, 2011.
- [20] Robert Hibbins. Information provided by supervisor.
- [21] W.K. Hocking. http://www.physics.uwo.ca/~whocking/p103/grav_wav.html.
- [22] M.J. Taylor K.Nielsen and M.J. Jarvis R.E. Hibbins. Climatology if short-period mesospheric gravity waves over halley, antartica (76s,27w). *Journal of Atmospheric and Solar-Terrestrial Physics*, 2009.
- [23] Harald Lund. Variation of the hydroxyl near infrared airglow at rothera antartica(68s,68w). Master's thesis, NTNU, 2010.
- [24] Theodore Tantaló Robert D.Fiete. Comparison of snr image quality metric for remote sensing systems. *Optical Engineering*, 2000.
- [25] Gaute Bråthen. -. Master's thesis, NTNU, 2012.
- [26] Kimberly M. Vogt Thomas J. Fellers and Michael W. Davidson. <http://www.microscopyu.com/tutorials/java/digitalimaging/signaltonoise/index.html>.